Global and Planetary Change xxx (2012) xxx–xxx

Contents lists available at SciVerse ScienceDirect

Global and Planetary Change

journal homepage: www.elsevier.com/locate/gloplacha

Volcanism in South China during the Late Permian and its relationship to marine ecosystem and environmental changes

Jun Shen [a], Thomas J. Algeo [b], Qing Hu [a,c], Guozhen Xu [a], Lian Zhou [a], Qinglai Feng [a,*]

[a] State Key Laboratory of Geological Process and Mineral Resources, China University of Geosciences, Wuhan, Hubei 430074, PR China
[b] Department of Geology, University of Cincinnati, Cincinnati, OH 45221-0013, USA
[c] Key Laboratory of Earthquake Geodesy, Institute of Seismology, CEA, Wuhan, 430071, China

ARTICLE INFO

Article history:
Received 28 April 2011
Accepted 22 February 2012
Available online xxxx

Keywords:
Permian–Triassic
mass extinction
primary productivity
anoxia
rare earth elements
chemical index of alteration

ABSTRACT

A deep-shelf section at Xinmin (Guizhou Province, South China) records numerous volcanic ashfall events both preceding and following the latest Permian mass extinction. Each ash layer was associated with ecosystem and environmental changes, including significant declines in biogenic silica and carbonate production and shifts toward somewhat more reducing conditions within a generally suboxic facies. The extinction horizon itself, which coincided with an ashfall event, shows evidence of much larger changes, including a sharp and sustained reduction in radiolarian productivity, a shift from suboxic to mostly oxic conditions (although punctuated by episodic euxinic events), and an increase in weathering intensity due to increased climatic humidity. Ash layers of Late Permian–Early Triassic age at Xinmin and elsewhere in South China are thought to have had a regional volcanic source, perhaps in subduction-zone magmatic arcs along the margins of the South China Craton. The Xinmin section provides evidence that volcanically generated stresses were repeatedly imposed on marine systems of the South China Craton during the Late Permian, possibly weakening their resilience in advance of the Permian–Triassic boundary crisis.

1. Introduction

The ~252-Ma latest Permian mass extinction (LPME) was the most severe biotic crisis of the Phanerozoic (Erwin et al., 2002), yet its dynamics and underlying causes remain under debate. The ultimate cause of this boundary event is thought to have been large-scale eruptions of flood basalts of the Siberian Traps, radiometric dating of which has shown to be effectively coeval with the Permian–Triassic boundary (PTB) (Campbell et al., 1992; Renne et al., 1995; Kamo et al., 2003; Reichow et al., 2009). The PTB crisis is associated with volcanic ash layers in the Global Stratotype Section and Point (GSSP) at Meishan D in eastern China (Jin et al., 2000; Yin et al., 2001, 2007). These ash layers increase in number and thickness to the south and southwest (paleo-coordinates) across the South China Craton (Yin et al., 1992; Tong et al., 2007; Xie et al., 2010). They are thus thought to be unrelated to the Siberian Traps and of regional origin, possibly sourced in a volcanic arc on the southern paleomargin of the South China Craton (Yin et al., 1992). Because these ash layers are correlative with the main extinction horizons, i.e., Beds 25 and 28 at Meishan D (Jin et al., 2000; Xie et al., 2010), it appears that regional volcanism may have contributed to the PTB biotic crisis in South China.

In the present study, we investigated the relationship of volcanism in the South China region to marine biotic and environmental conditions during the latest Permian. The Xinmin section in Guizhou Province was chosen because (1) its paleogeographic location was relatively close to the inferred source of volcanic activity on the southern paleomargin of the South China Craton, and (2) its deepwater setting in the Nanpanjiang Basin was favorable for recording continuous sedimentation with minimal bioturbation or other post-depositional disturbances. Further, while shallow-marine and intermediate-depth sections in South China have been the subject of many earlier geochemical studies (e.g., Grice et al., 2005; Xie et al., 2005, 2007, 2010; Algeo et al., 2007a, 2008; Cao et al., 2009), deep-water facies have received far less attention to date (e.g., Shen et al., 2012). The results of the present chemostratigraphic study of the Xinmin section provide new insights concerning the occurrence of volcanic activity in the South China region during the latest Permian and its relationship to contemporaneous changes in marine ecosystems and environmental conditions.

2. Geological setting and stratigraphy

The South China Craton was located in the Paleo-Tethys Ocean near the paleo-equator during the Permian–Triassic (Fig. 1A). The deep-water Nanpanjiang Basin developed on the craton's southern margin during the Permian and differentiated into shallow carbonate platform, slope, and basinal environments by the Early Triassic (Enos

---

* Corresponding author. Tel.: +86 18971193331.
E-mail address: qinglaifeng@cug.edu.cn (Q. Feng).

0921-8181/$ – see front matter © 2012 Published by Elsevier B.V.
doi:10.1016/j.gloplacha.2012.02.011

Please cite this article as: Shen, J., et al., Volcanism in South China during the Late Permian and its relationship to marine ecosystem and environmental changes, Glob. Planet. Change (2012), doi:10.1016/j.gloplacha.2012.02.011

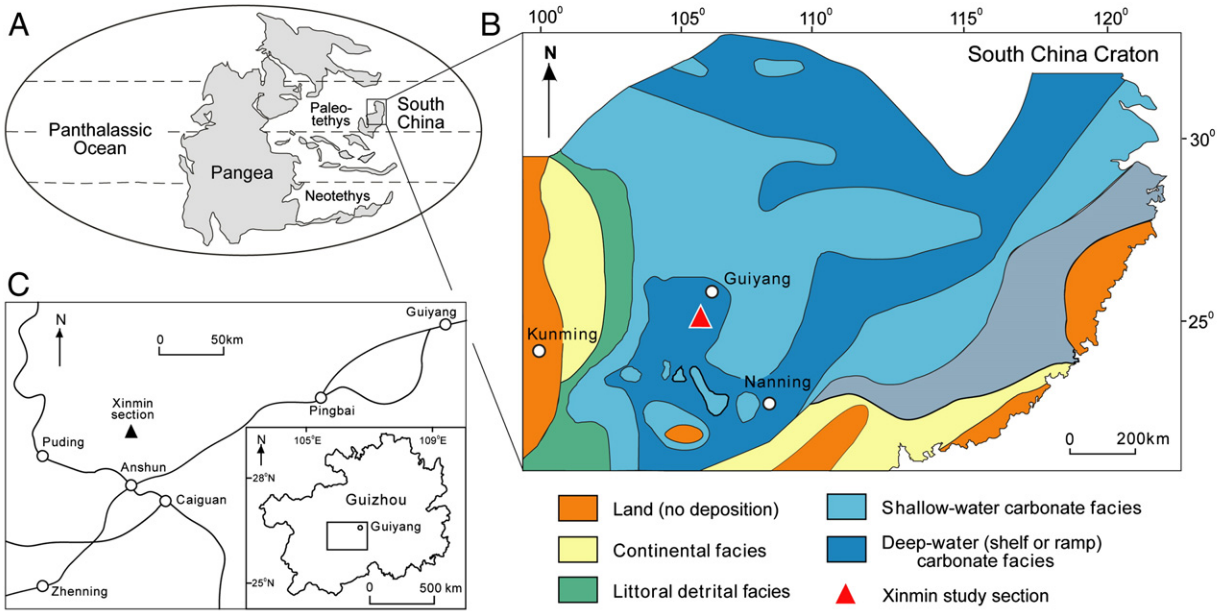

Fig. 1. (A) Global paleogeographic reconstruction during the Permian–Triassic transition. Base map courtesy of Ron Blakey (http://jan.ucc.nau.edu/~rcb7/). (B) Paleogeography of South China during the latest Permian (modified after Feng and Gu, 2002). (C) Location map of Xinmin section.

et al., 2006). Many sections in this region provide a continuous record of sedimentation across the PTB (Yang et al., 1987; He et al., 2005; Feng et al., 2007). Sections recording basinal facies typically contain well-preserved radiolarian cherts and siliceous mudstones (assigned to the latest Permian Dalong Formation and its stratigraphic equivalents), overlain by poorly fossiliferous siliceous mudstones (corresponding to the earliest Triassic Luolou Formation and its stratigraphic equivalents; Fig. 1B). The water depth of the basinal facies has been estimated at 200–500 m (Lai et al., 2001; He et al., 2005).

We investigated the deep-water Xinmin section, located ~30 km north of Anshun City in Guizhou Province (Fig. 1C). The section can be divided on the basis of lithology and bedding characteristics into three lithostratigraphic units. The ~8-m-thick lower unit (Beds 1–5) consists of argillaceous limestone and siliceous to calcareous mudstone with abundant radiolarian, ammonoid, brachiopod, and plant fossils (Fig. 2). This unit contains at least 9 discrete claystone beds that represent volcanic ash layers (or composite layers) from 10 to 40 cm in thickness (Fig. 2A–B). Many ash layers are underlain by a 10- to 20-cm-thick calcareous mudstone or limestone bed and overlain by a thin (few mm) black shale. The ~1.3-m-thick middle unit (Beds 6–8) consists of siliceous mudstone with interbeds of volcanic ash. The ~2-m-thick upper unit (Bed 9) consists mainly of yellowish thin-bedded siliceous mudstone. The middle and upper units contain few fossils and do not show distinct rhythmic bedding of the type found throughout the lower unit (Fig. 2C–D). In addition to the discrete ash layers identified in Fig. 2 and other figures, unsampled thin ash layers are present within the study section.

Conodonts are the standard marine microfossil for Permian–Triassic biostratigraphic correlations, although radiolarians are useful also in deep-water facies. The PTB is formally designated at the base of the *Hindeodus parvus* zone in the Meishan GSSP (Yin et al., 2001). At Xinmin, *H. parvus* has not been recovered, but other fossil finds allow approximate placement of the PTB. The upper part of Bed 5 yielded the conodont *Clarkina meishanensis*, the ammonoid *Huananoceras* sp., and the bivalve *Claraia primitiva* Yin, an assemblage that confirms the latest Changhsingian age of this unit (Q.L. Feng, unpubl. data). Recovery of a specimen of the ammonoid *Ophiceras* sp. from near the base of Bed 6 may indicate that the PTB is within the 15 cm of section overlying the Bed 5/6 contact (Fig. 2); however, further fossil finds are needed to corroborate this placement.

3. Methods and materials

Samples were trimmed to remove visible veins and weathered surfaces, and pulverized to ~200 mesh size in a tungsten ball mill. Ten samples distributed throughout the study section were selected for whole-rock X-ray diffraction (XRD) analysis (n.b., clay-fraction analysis was not performed). Powdered samples were placed in aluminum holders and scanned using a D/max-3B X-ray diffractometer at the State Key Laboratory of Geological Processes and Mineral Resources, China University of Geosciences (Wuhan). Samples were scanned from 2° to 32° 2θ at 0.2° min^{-1} using CuKα radiation and a graphite monochromator.

C and S elemental concentrations were measured using an Eltra 2000 C-S analyzer at the University of Cincinnati. Data quality was monitored via multiple analyses of USGS SDO-1 standard, yielding an analytical precision (2σ) of $\pm 2.5\%$ of reported values for C and $\pm 5\%$ for S. An aliquot of each sample was digested in 2 N HCl at 50 °C for 6 h to dissolve carbonate minerals, and the residue was analyzed for total organic carbon (TOC) and non-acid-volatile sulfur (NAVS); total inorganic carbon (TIC) and acid-volatile sulfur (AVS) were obtained by difference.

Trace-element and REE abundances were measured by Agilent 7500a inductively coupled plasma mass spectrometry (ICP-MS) at the State Key Laboratory of Geological Processes and Mineral Resources, China University of Geosciences (Wuhan). About 50 mg of each sample powder was weighed into a Teflon bomb and then moistened with a few drops of ultra-pure water before addition of 1 mL HNO_3 and 1 mL HF. The sealed bomb was heated at 190 °C in an oven for more than 48 h. After cooling, the bomb was opened and evaporated at 115 °C to incipient dryness, then 1 mL HNO_3 was added and the sample was dried again. The resultant salt was re-dissolved with 3 mL 30% HNO_3 before it was again sealed and heated in the bomb at 190 °C for 12 h. The final solution was transferred to a polyethylene bottle and diluted in 2% HNO_3 to about 80 mL for ICP-MS analysis. Analysis of the international rock standards BHVO-2 and BCR-2 indicated that analytical precision was mostly better than 5%, according to the relative standard deviation (RSD).

Major-element abundances were determined by wavelength-dispersive X-ray fluorescence (XRF) analysis on fused glass beads using an XRF-1800 at the Key Laboratory of Biogeology and Environmental

Please cite this article as: Shen, J., et al., Volcanism in South China during the Late Permian and its relationship to marine ecosystem and environmental changes, Glob. Planet. Change (2012), doi:10.1016/j.gloplacha.2012.02.011

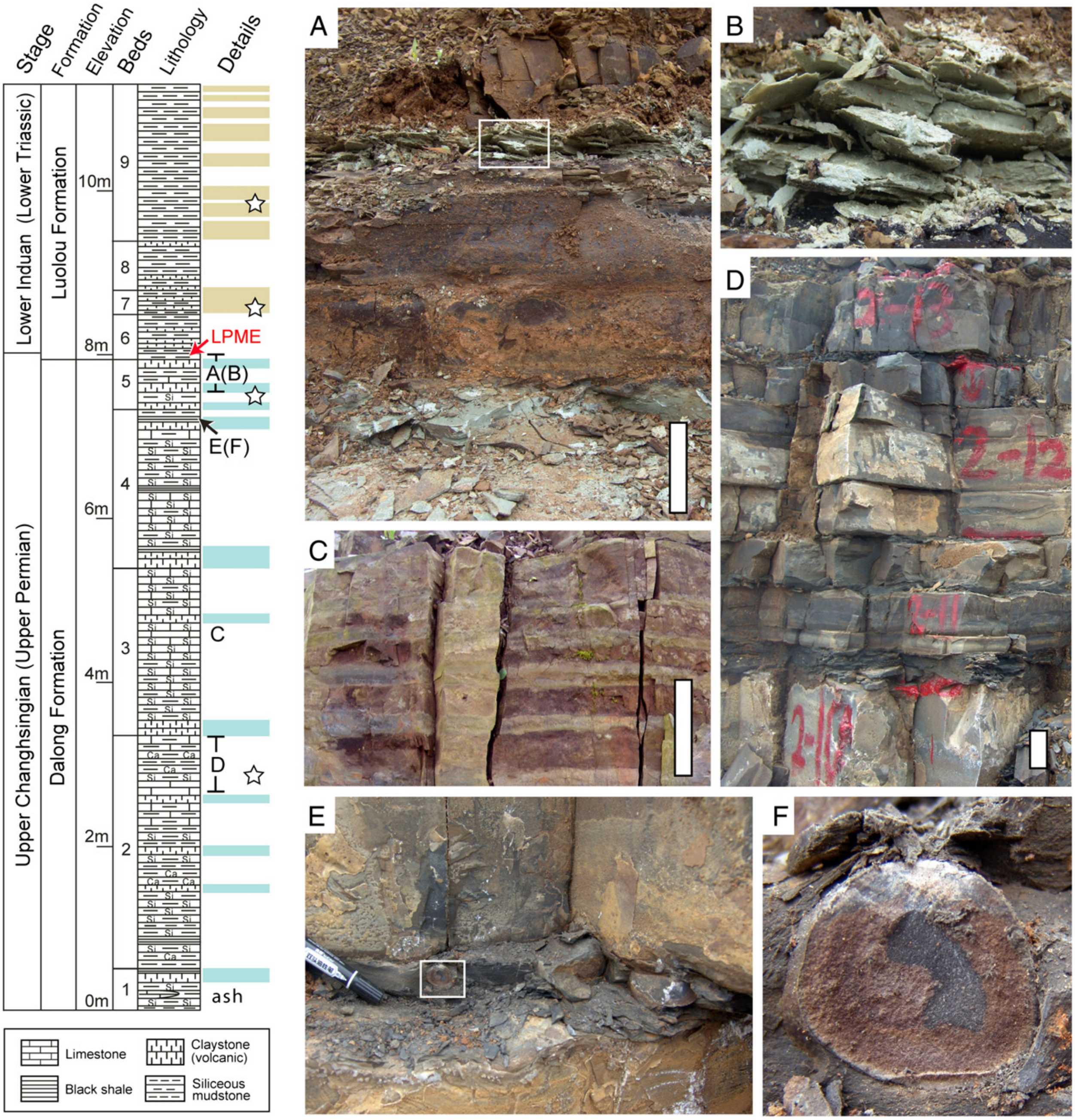

Fig. 2. Xinmin measured section and field photos: (A) Volcanic ash layers in Unit 5. (B) Close-up of volcanic ash layer in A (inset rectangle). (C) Rhythmic siliceous mudstones in Unit 3. (D) Thinly bedded calcareous and siliceous mudstones of Unit 2. (E) Phosphatic mudstone near top of Unit 4. (F) Detail of phosphate nodule in E (inset rectangle). Scale bars in A–C–D equal 10 cm. In the Details column, A to F show positions of samples in field photos, and stars show positions of the four XRD samples in Fig. 3. The blue bars represent volcanic ash layers recognized in field, and the brown bars represent ash layers inferred on the basis of mineralogic and geochemical data (see Figs. 4 and 6A). Note that not all ash layers present in the section were sampled. Abbreviations: LPME = latest Permian mass extinction horizon; (lithologies) Ca = calcareous and Si = siliceous. (For interpretation of the references to color in this figure legend, the reader is referred to the web version of this article.).

Geology of the Ministry of Education, China University of Geosciences (Wuhan). The fractions of the major mineral components of each sample were determined through reduction of major-element and TIC data as follows (cf. Algeo et al., 2007b):

$$\text{Illite}(\%) = m \times K_2O \times 100/\kappa_1 \qquad (1)$$

$$\text{Chlorite}(\%) = (Al_2O_3 - (m \times K_2O)) \times 100/\kappa_2 \qquad (2)$$

$$\text{Biogenic SiO}_2(\%) \qquad (3)$$
$$= SiO_{2(\text{total})} - (m \times K_2O \times 2.36) - ((Al_2O_3 - m \times K_2O) \times 1.18)$$

$$\text{Calcite}(\%) = TIC \times 100/12.0 \qquad (4)$$

where m is the slope of the Al_2O_3–K_2O regression, the constants κ_1 and κ_2 represent the average concentrations of Al_2O_3 in illite (25%) and chlorite (21%), respectively, the coefficients 2.36 and 1.18 represent the weight ratios of $SiO_2/(0.5 \times Al_2O_3)$ in clay minerals of stoichiometric composition having TOT and TOTO structures (i.e., illite and chlorite), respectively, the coefficient 12.0 represents the molar weight in grams of carbon in $CaCO_3$, and TIC is the total inorganic carbon. For the 139 study samples, the procedure above yielded a mean sum of the four major mineral components of 99.4% with a standard deviation of 4.3%; for purposes of presentation, the component fractions for each sample were normalized to 100%.

The principles underlying the calculations above are that (1) total Al is apportioned among the two clay–mineral phases (illite and chlorite) based on K concentrations (cf. Srodon, 2009); (2) Al concentrations are converted to clay–mineral abundances based on average mineral-specific Al_2O_3 values given in Grim (1968); and (3) biogenic SiO_2 (=chert) is the amount of SiO_2 remaining after subtracting the estimated SiO_2 concentrations of the two clay–mineral phases. Regarding the apportionment of Al, this procedure makes use of the fact that the major silica-bearing mineral phases present (i.e., illite, chlorite, and chert) exhibit different Si:Al ratios. Illite and chlorite have molar Si:Al ratios of 2:1 and 1:1, respectively, owing to their different layer structures (TOT versus TOTO), and chert contains no structural Al. The strong correlation of K_2O with Al_2O_3 ($r^2=0.97$ and 0.92 for pre-LPME and post-LPME samples, respectively; Fig. 5A) demonstrates that nearly all K is resident in illite. K-feldspar is unlikely to contribute any significant quantity of K to the samples because (1) XRD traces show no evidence of this mineral phase, and (2) weight ratios of K_2O:Al_2O_3 for Upper Permian (0.28) and Lower Triassic (0.41) samples (Fig. 5A) are much closer to those for illite (0.2–0.3) than for K-feldspar (0.92) (Grim, 1968). Thus, the amount of Al_2O_3 in the illite phase can be estimated from total K_2O content as $m \times K_2O$, where m is 3.49 and 2.24 for pre-LPME and post-LPME samples, respectively (Fig. 5A), and the amount of Al_2O_3 in the chlorite phase is determined by difference (i.e., $Al_2O_{3\,(total)} - Al_2O_{3\,(illite)}$).

The amount of SiO_2 in the illite and chlorite phases was estimated from measured Al_2O_3 data and published mineral-specific SiO_2:Al_2O_3 ratios (Grim, 1968), and the residual SiO_2 was assigned to the chert fraction. Regarding the origin of the residual SiO_2, Eq. (3) cannot distinguish between primary biogenic silica, diagenetic silica (chert), and detrital silica (mineral quartz). However, field and petrographic observations preclude the presence of detrital quartz grains larger than silt, and earlier studies have demonstrated an abundance of radiolarian fossils in this section and others in the Nanpanjiang Basin (Feng and Gu, 2002; Feng et al., 2007; Shen et al., 2012). We infer that residual SiO_2 in the study section represents silica that is ultimately of biogenic (radiolarian) origin and that has now largely recrystallized to chert (cf. DeMaster, 2004). Because the amount of biogenic silica determined by the procedure above generally equals or exceeds the amount of SiO_2 in the two clay–mineral phases, minor uncertainties in the latter do not greatly affect estimates of the former.

The chemical index of alteration (CIA) was calculated using weight fractions of major-element oxides as follows (cf. Price and Velbel, 2003):

$$CIA = Al_2O_3/(Al_2O_3 + K_2O + Na_2O + CaO_{noncarb}) \qquad (5)$$

where $CaO_{noncarb}$ represents the weight fraction of CaO present in non-carbonate phases, which was calculated as $CaO_{total} - TIC \times 56.1/12.0$, where 56.1 and 12.0 are the molar weights in grams of CaO and C, respectively.

The magnetic susceptibility (MS) of samples was measured using a high-sensitivity susceptibility bridge at the China University of Geosciences (Wuhan). The susceptibility bridge was calibrated using standard salts, for which values are given in Swartzendruber (1992).

4. Results

4.1. Mineralogic analysis

XRD data demonstrate that the main mineral phases at Xinmin are chert, calcite, illite, chlorite, and plagioclase (Fig. 3). The chert and calcite in deep-shelf facies of the Nanpanjiang Basin are inferred to be of dominantly biogenic origin (Feng and Gu, 2002; Feng et al., 2007; Shen et al., 2012). The clay minerals and feldspars are of detrital and, in part, volcanoclastic origin (see below). The association of illite with the volcanic fraction at Xinmin reflects the transformation of volcanic glass fragments (ash) first to zeolite and smectite (Hodder et al., 1993; Masuda et al., 2001) and ultimately to illite or mixed-layer illite/smectite (Bethke et al., 1986; Drits et al., 1997). Although illite and smectite cannot be distinguished on the basis of XRD analysis (Srodon et al., 2001; Srodon, 2009), major-element geochemistry (Section 3) suggests that the 2:1-layer clay–mineral fraction at Xinmin consists dominantly of illite or mixed-layer illite/smectite rather than smectite.

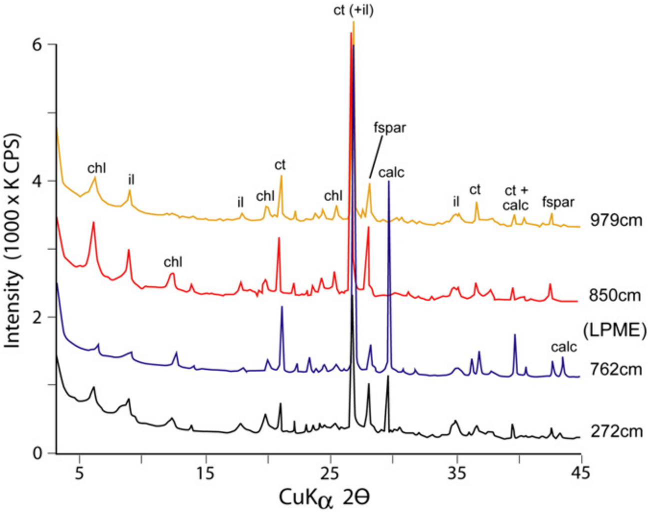

Fig. 3. XRD diffractograms for selected whole-rock samples. Samples identified by elevation within section; the latest Permian mass extinction (LPME) horizon is located at ~790 cm, between samples 762 cm and 850 cm; see Fig. 2 for reference. Abbreviations: calc = calcite, chl = chlorite, ct = chert, il = illite, and plag = plagioclase.

The XRD data show some stratigraphic variation in the major mineral phases: chert declines and calcite disappears above the LPME (samples 850 cm and 979 cm), whereas chlorite and plagioclase become more abundant, especially just above the LPME (sample 850 cm; Fig. 3). However, stratigraphic variation in the major mineral phases can be assessed more fully on the basis of reduced geochemical concentration data (Eqs. 1–4). The numerous volcanic ash layers below the LPME in the Xinmin section are associated with substantial changes in mineralogy (Fig. 4). Each ash layer exhibits a large decrease in chert and calcite abundance and a corresponding increase in illite, while chlorite abundance varies comparatively little. Covariation among these major mineral phases is strong: illite covaries negatively with chert ($r=-0.90$; $n=99$) and calcite ($r=-0.76$), and chert covaries positively with calcite ($r=0.45$; Fig. 5B), while chlorite shows no statistically significant relationship to the other mineral fractions (but see Section 4.2). Illite is the dominant mineral phase in the ash layers; although potentially of detrital origin, most of the illite is inferred to be ultimately of volcanic origin because the sediment layers with the smallest volcanic ash fraction (as proxied by Eu/Eu*; Section 4.2) contain only ~10 ± 10% illite.

Above the LPME, calcite disappears and the remaining mineral phases exhibit reduced sample-to-sample variation. No samples show the illite-dominated composition (or low Eu/Eu* values; Section 4.2) typical of the volcanic ash layers below the LPME. Although field and petrographic observations indicate the presence of some volcanogenic material in Beds 6–9, it is not present as discrete ash layers but, rather, as a subordinate component in siliceous mudstone beds of predominantly detrital origin (see Section 5.1.3). The bulk mineralogy of the Xinmin section changes across the LPME horizon. Pre-LPME samples have an average composition of 42 ± 28% illite, 31 ± 21% chert, 16 ± 6% chlorite, and 11 ± 12% calcite. Post-LPME samples average 40 ± 19% illite, 30 ± 11% chert, 30 ± 9% chlorite, and 0% calcite. The major changes are thus a large increase in chlorite and a corresponding

Please cite this article as: Shen, J., et al., Volcanism in South China during the Late Permian and its relationship to marine ecosystem and environmental changes, Glob. Planet. Change (2012), doi:10.1016/j.gloplacha.2012.02.011

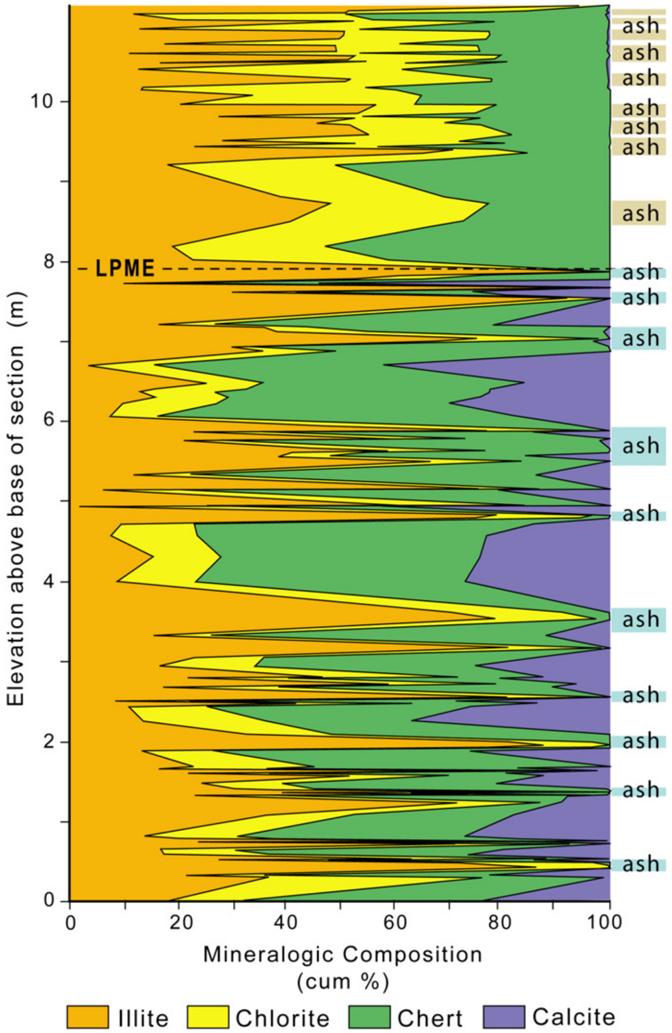

Fig. 4. Stratigraphic variation in main mineral fractions (calculated from Eqs. (1)–(4) of text). The blue bars represent volcanic ash layers recognized in field, and the brown bars represent ash layers inferred on the basis of mineralogic and geochemical data. LPME = latest Permian mass extinction horizon. (For interpretation of the references to color in this figure legend, the reader is referred to the web version of this article.).

decrease in calcite. Above the LPME, patterns of covariation among the major mineral phases change somewhat: although illite continues to covary negatively with chert ($r = -0.92$; $n = 45$), the only other significant relationship is negative covariation between illite and chlorite ($r = -0.35$).

4.2. Chemostratigraphic profiles

The single best proxy for volcanic ash content at Xinmin is Eu/Eu*, as shown below. Beneath the LPME, ash layers form discrete beds that are easily recognized in the field (Fig. 2), and all such layers yield Eu/Eu* values that are much lower (0.2–0.8) than those of the interbedded mudstones (~1.0 ± 0.2; Fig. 6A). Further, Eu/Eu* covaries strongly with all of the major mineral phases, yielding correlation coefficients (r) of −0.57 with illite, +0.45 with chert, and +0.53 with calcite. These relationships are consistent with the inference that ash layers, which are rich in illite and poor in chert and calcite (Section 4.1), are characterized by low Eu/Eu* values. The relationship of Eu/Eu* to volcanic ash content is less obvious above the LPME because the ash layers are more numerous, less distinct, and different in chemical composition from those below the LPME. Above the LPME, the Eu/Eu* profile exhibits a sustained shift toward higher values, averaging ~1.2 and rising to a maximum of ~1.7 (Fig. 6A). Nonetheless, lower Eu/Eu* values continue to characterize layers with a large volcanic ash component, as shown by covariation of Eu/Eu* with the major mineral phases yielding correlation coefficients (r) of −0.61 with illite, +0.50 with chert, and +0.42 with calcite. These relationships are almost identical to those below the LPME (see above), demonstrating that, despite a large shift in Eu/Eu* values above the LPME, the relatively lower values (<1.2) continue to characterize layers with a large volcanic ash component.

Below the LPME, most variation in chemostratigraphic profiles is controlled by the fraction of volcanic ash in the sediment. Each ash layer shows a sharp increase in Al_2O_3 (Fig. 6B), which is associated with greater illite abundance (Section 4.1; cf. Huff et al., 1991, 2000). Above the LPME, mean Al_2O_3 concentrations are about the same as below the LPME but variance is reduced by approximately a factor of three. The chemical index of alteration (CIA) averages 0.77 ± 0.05 below the LPME with higher values associated with ash layers (Fig. 6C). Given the aluminous composition of the ash layers (Fig. 6A), CIA values may reflect the fraction of volcanic ash in a sample rather than the weathering intensity of the detrital fraction. Above the LPME, CIA shifts toward higher values, ranging from 0.75 to 0.90 with a mean value of ~0.81 (Fig. 6C). This shift is unlikely to reflect an increase in the proportion of volcanic ash in the sediment because (1) mean Al_2O_3 content remains unchanged (Fig. 6B), and (2) Eu/Eu* shifts toward higher values (i.e., away from the volcanic ash endmember; Fig. 6A). Thus, the shift toward higher CIA values above the LPME may reflect changes in weathering intensity (Price and Velbel, 2003), consistent with other lines of evidence (see Section 5.1.3).

Fe concentrations below the LPME fluctuate between ~1.5% and 5%, with higher values associated with the ash layers (Fig. 6D). In this interval, Fe covaries positively with Al_2O_3, yielding $r = +0.46$ (Fig. 5C). Fe concentrations increase sharply across the LPME, averaging ~7 ± 2% in Beds 6–9 (Fig. 6D), and shift to a pattern of negative covariation with Al_2O_3 ($r = -0.64$; Fig. 5C). Because S concentrations are uniformly low throughout the section (<0.1%; Fig. 6G), Fe is not associated to any significant degree with pyrite. Rather, Fe is inferred to reside primarily in a Fe-chlorite phase that is present throughout the section but that increases sharply in abundance above the LPME. Fe shows statistically significant covariation with chlorite abundance (as determined by XRD), yielding $r = +0.46$ and +0.65 below and above the LPME, respectively. Furthermore, the strength of this correlation improves markedly (to $r = +0.55$ and +0.72 below and above the LPME, respectively) for Fe + Mg (molar) versus chlorite (Fig. 5D). These relationships suggest that most Fe and Mg are resident in chlorite throughout the study section, and that Fe substitutes for Mg in the chlorite crystal lattice. Because Fe shifts from positive covariation with illite below the LPME ($r = +0.71$) to negative covariation above the LPME ($r = -0.82$), it appears that the Fe-chlorite phase is associated with volcanic ash layers below the LPME (cf. Masuda et al., 2001) but with comparatively ash-poor beds above the LPME (Fig. 4).

A single sample at 133 cm is super-enriched in Fe (18.5%; Fig. 6D). The same sample is also strongly enriched in Pb, Zn, Ni, Mo, and Co (by a factor of >10× relative to section-mean values; data not shown), suggesting some mechanism of metal concentration (e.g., submarine hydrothermal input, or accumulation on a submarine hardground surface) that was not otherwise operative at Xinmin. Fe_T/Al, a widely used paleoredox proxy, ranges from ~0.2 to 2.2 (Fig. 6E). Because other proxies do not provide evidence of strong redox variation in the study section (see Section 5.1.2), the Fe_T/Al profile probably reflects variable admixture of the Fe-chlorite phase discussed above rather than redox fluctuations. This observation suggests the need for caution in utilizing Fe_T/Al in paleoredox analysis.

Magnetic susceptibility (MS) varies mostly in the range of 20 to 100 SI below the LPME, with distinctly higher values associated

Please cite this article as: Shen, J., et al., Volcanism in South China during the Late Permian and its relationship to marine ecosystem and environmental changes, Glob. Planet. Change (2012), doi:10.1016/j.gloplacha.2012.02.011

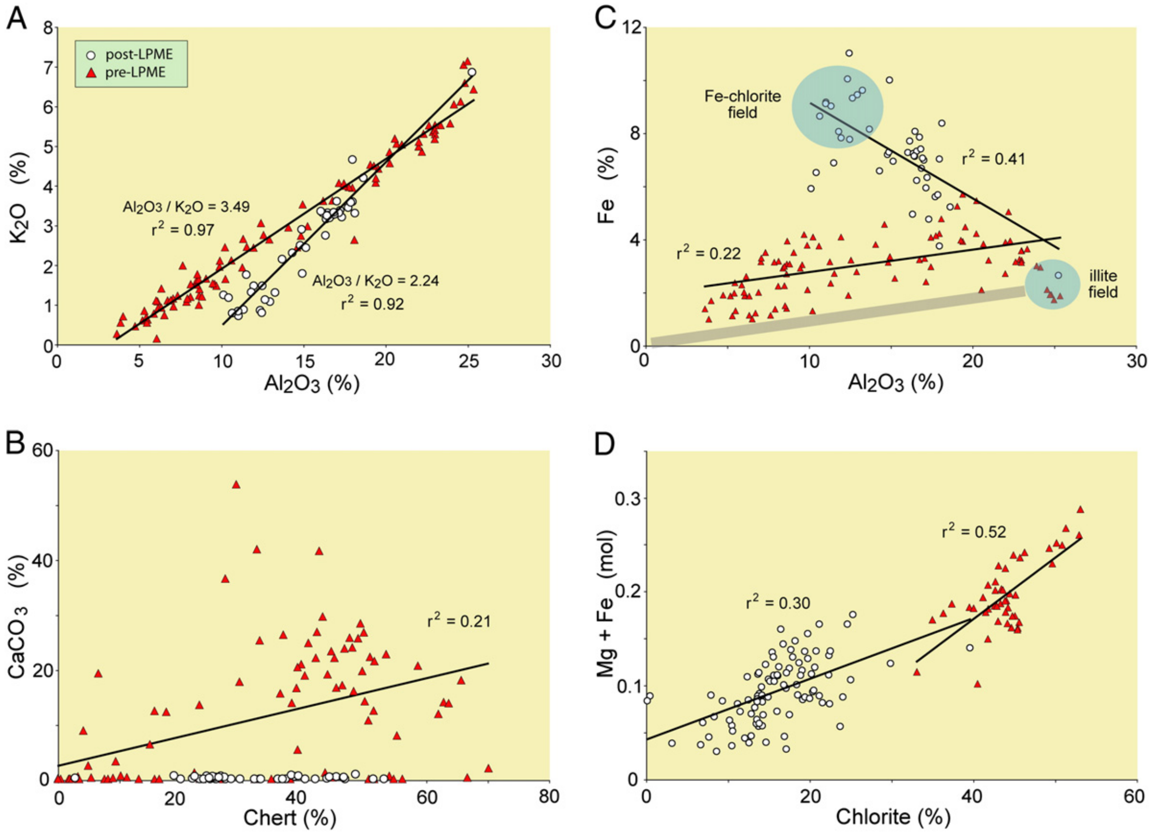

Fig. 5. Crossplots of (A) K_2O versus Al_2O_3, (B) $CaCO_3$ versus chert, (C) Fe versus Al_2O_3, and (D) molar Mg + Fe versus chlorite. In C, the gray diagonal line represents a mixing trend between non-aluminous components (e.g., chert and calcite) and illite having an endmember composition of ~2% Fe and ~25% Al_2O_3 (illite field); samples plotting above this line contain proportionately larger amounts of an Fe-chlorite phase, which is inferred to have an end-member composition of ~8–10% Fe and ~10–14% Al_2O_3 (chlorite field). Post-LPME samples largely represent a two-component mixing system between illite and Fe-chlorite. See text for discussion of significance of each panel. LPME = latest Permian mass extinction.

with each ash layer (Fig. 6F). The relatively high MS of the ash layers may be due to greater concentrations of paramagnetic clay minerals such as illite or Fe-chlorite (Fig. 4). Because illite and Fe exhibit positive covariation below the LPME (see above), their relative contributions to the MS signal cannot be separated. A trend toward higher MS values is evident above the LPME, reaching a maximum in Bed 9 where MS averages ~125 SI and ranges up to ~200 SI (Fig. 6F). Because illite and Fe exhibit negative covariation above the LPME (see above), their relative contributions to the MS signal of this interval can be determined. The MS profile matches the illite profile (Fig. 4) more closely than the Fe profile (Fig. 6D), suggesting that paramagnetic illite is the dominant contributor to the MS signal (cf. Ellwood et al., 2000, 2008).

Sulfur (S) concentrations are uniformly low (<0.1%) throughout the study section (Fig. 6G). Phosphorus (P) concentrations are also low (<0.2%) through most of the study section, although a few peaks (to >0.5%) are found in beds immediately overlying some volcanic ash layers (Fig. 6H). In addition, P concentrations increase somewhat upsection, averaging ~0.05% below the LPME versus ~0.15% above it.

Total organic carbon (TOC) concentrations are low (<1%) through most of the section (Fig. 7A). Higher TOC values (to 3.1%) are found mainly in the thin black shales capping some volcanic ash layers below the LPME. Above the LPME, TOC values are uniformly low (<0.3%). Organic carbon $\delta^{13}C$ ranges from about −29‰ to −23‰, with shifts of −2 to −6‰ associated with each volcanic ash layer (Fig. 7B). The C-isotope excursions are found within the ash beds in Bed 1 to lower Bed 4 (i.e., not associated with the capping black shale), although excursions occur at the tops of ash layers in the upper part of Bed 4 and in Bed 5 (i.e., in the capping black shale). A persistent negative trend in $\delta^{13}C_{org}$ commences at the LPME, producing the most ^{13}C-depleted values (−29.1‰) near the top of Bed 8 (Fig. 7B). This trend represents the negative shift observed at the level of the LPME in both carbonate and organic $\delta^{13}C$ profiles globally (e.g., Baud et al., 1989; Horacek et al., 2007; Tong et al., 2007; Algeo et al., 2012a).

$CaCO_3$ concentrations (=calcite; Eq. (4)) average ~20% (range ~0 to 55%) in the mudstones below the LPME (Fig. 7C). The volcanic ash layers below the LPME contain no $CaCO_3$, nor do the mudstone layers above the LPME. Chert concentrations average ~40% (range ~10 to 70%) in the mudstones below the LPME (Fig. 7D). The volcanic ash layers below the LPME mostly contain small amounts of chert (<10%). The mudstones above the LPME average ~30% chert but show markedly less variation (range ~15 to 45%) than the mudstones below the LPME. Below the LPME, chert covaries positively with $CaCO_3$, yielding $r = +0.45$ (Fig. 5B). We infer that this relationship represents coordinated variation in productivity among carbonate and siliceous plankton. Above the LPME, an absence of $CaCO_3$ precludes any covariation with chert.

Molybdenum (Mo) exhibits mostly low concentrations (<1 ppm) below the LPME, although with a spike to 24 ppm in conjunction with the Fe-enriched bed at 133 cm discussed above (Fig. 7E). Above the LPME, Mo increases to >4 ppm in some of the mudstone interbeds between ash layers. Mo variation in the study section is not simply the product of variable input of detrital Mo, as shown by normalization of Mo concentrations to Al (Fig. 7F). Rather, we interpret variations in Mo at Xinmin to reflect minor fluctuations in depositional redox conditions (see Section 5.1.2). Uranium (U) concentrations range up to 25 ppm, although all values >10 ppm are associated with volcanic ash layers below the LPME (Fig. 7G). The strength of this association and the somewhat bimodal distribution of U concentrations below

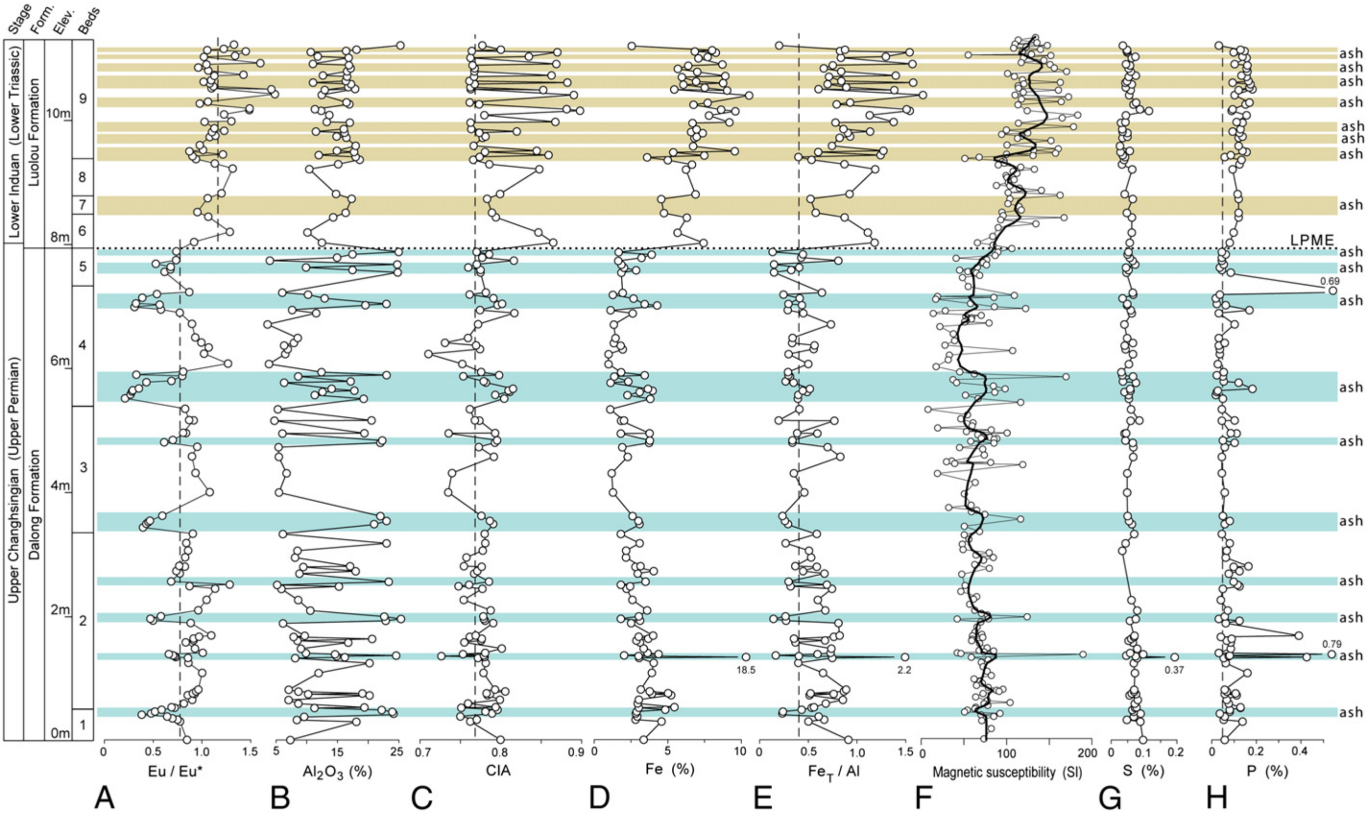

Fig. 6. Chemostratigraphic profiles: (A) Eu/Eu*, (B) Al_2O_3, (C) CIA (chemical index of alteration; calculated from Eq. (5) of text), (D) total Fe, (E) Fe_T/Al, (F) magnetic susceptibility (MS), (G) S, and (H) P. Dashed lines represent (A) threshold Eu/Eu* values for volcanic ash layers are 0.8 below the LPME and 1.2 above the LPME; (C) pre-LPME mean CIA (0.77); (E) average shale Fe_T/Al (0.40; Lyons and Severmann, 2006); and (H) pre-LPME baseline of 0.05% P. Note that the MS data were generated from an independently collected second sample suite and thus do not match the other profiles with regard to the number and stratigraphic position of samples. The blue bars represent volcanic ash layers recognized in field, and the brown bars represent ash layers inferred on the basis of mineralogic and geochemical data. LPME = latest Permian mass extinction horizon. (For interpretation of the references to color in this figure legend, the reader is referred to the web version of this article.)

the LPME suggest that the high U values reflect a provenance control (i.e., U-enriched volcanic ash) rather than a redox control.

Ce/Ce* ranges mostly from ~0.8 to 1.1 and averages ~1.0 below the LPME (Fig. 7H). Minor variation is observed between the volcanic ash layers and the interbedded mudstones, although the relationship is not consistent. A systematic pattern commences in Bed 5 and becomes more pronounced upsection, especially in Bed 9 where ash layers yield nearly uniform Ce/Ce* values of ~0.8 and mudstones yield values ranging from ~1.3 to 1.9 with a mean of ~1.6 (Fig. 7H). The study samples show characteristic rare-earth element distribution patterns that allow categorization into three groups showing systematic stratigraphic variation (Fig. 7J; see Section 4.3 for details).

4.3. Rare earth elements

The study samples show three rare earth element (REE) distribution patterns. Group 1 consists of samples with a pronounced negative Eu anomaly (Eu/Eu*<0.7; Fig. 8A), Group 3 consists of samples with paired positive Ce and Eu anomalies (Ce/Ce* and Eu/Eu* both >1.2; Fig. 8D), and Group 2 consists of the remaining samples, which have small or no Ce and Eu anomalies. Although Groups 1 and 3 are quite distinct, considerable overlap exists between Group 2a (Fig. 8B) and Group 2b (Fig. 8C), which are defined on the basis of stratigraphic position—being located, respectively, below and above the LPME. When sorted in this manner, some additional features of the REE distributions that are common to samples in each group become evident. Samples in Group 1 and (to a somewhat lesser degree) Group 2a exhibit peak REE concentrations toward the heavier end of the REE distribution, typically at the elements Tb or Dy. In contrast, samples in Groups 2b and 3 exhibit peak concentrations mostly at the element Eu, and concentrations fall off steeply toward the heavy end of the REE distribution (although some Groups 1 and 2a samples also show this pattern).

REE distributions at Xinmin vary systematically by lithology and stratigraphic position. Below the LPME, a dichotomy exists between the volcanic ash layers, most of which belong to Group 1, and the intervening mudstone layers, most of which belong to Group 2a (Fig. 7J). Above the LPME, the nature of the dichotomy in REE distributions shifts abruptly: samples containing greater amounts of volcanic ash belong mostly to Group 2b and the intervening mudstone layers mostly to Group 3. Similarities in the REE distributions between Groups 1 and 2a suggest some degree of sediment mixing, i.e., the ash layers contain some detrital siliceous material and the mudstone layers contain some volcanic ash. The same inference of sediment mixing applies to Groups 2b and 3. However, the substantial differences in REE distributions between samples from below the LPME (Groups 1 and 2a) and those from above the LPME (Groups 2b and 3) suggest that a major shift in the provenance and chemistry of both sediment fractions (i.e., volcanic ash and detrital siliciclastics) occurred at the LPME (Fig. 7J; see Section 5.1.3).

5. Discussion

5.1. Influence of volcanic events on marine environment

The influence of volcanic ashfall events on environmental conditions at Xinmin can be explored most easily by examining the relationship of Eu/Eu* to other sediment proxies. Although volcanic ash input influenced many aspects of sediment chemistry at Xinmin, Eu/Eu* is the most effective proxy for ash content (see Section 4.2), with values of <0.8 characteristic of ash layers below the LPME and values of <1.2

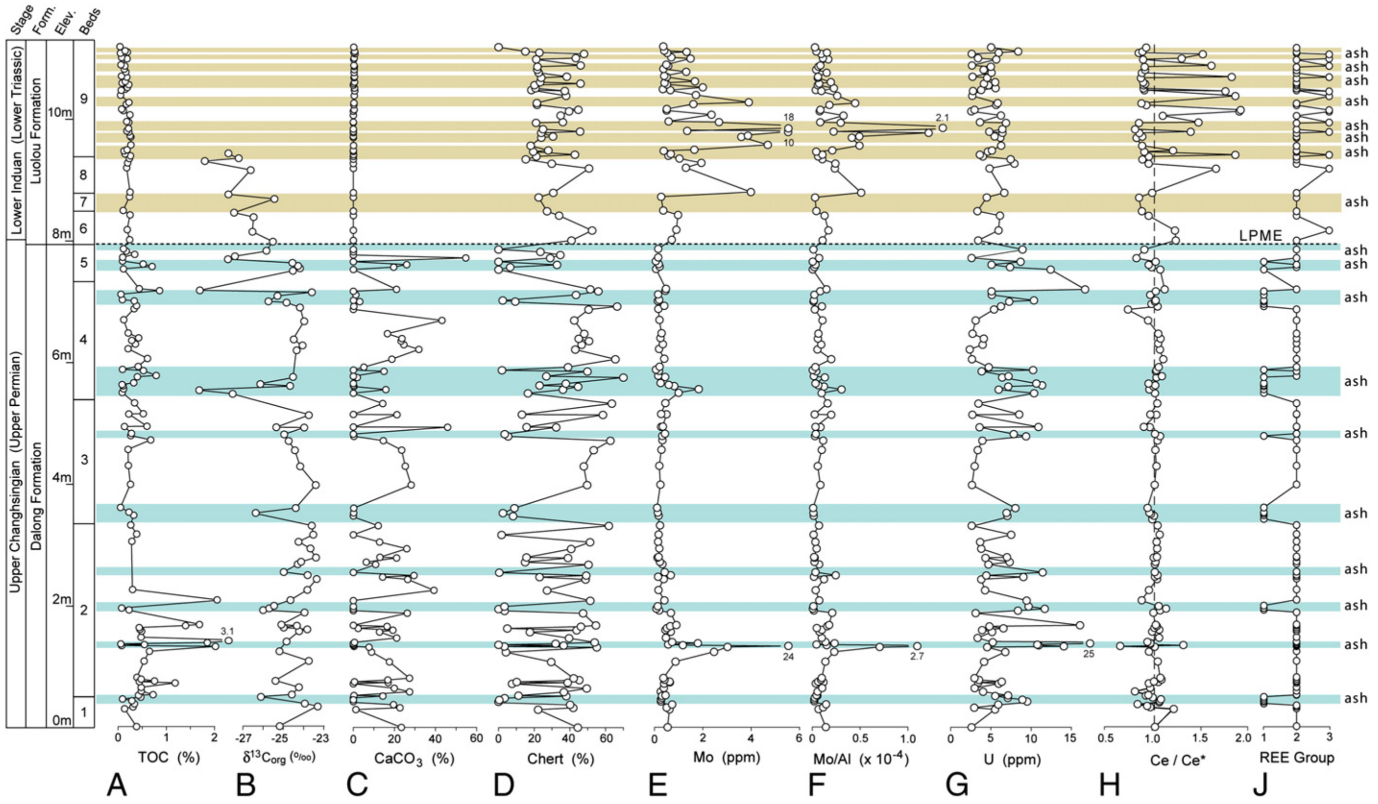

Fig. 7. Chemostratigraphic profiles: (A) TOC, (B) organic $\delta^{13}C$, (C) $CaCO_3$, (D) biogenic SiO_2, (E) Mo, (F) Mo/Al, (G) U, and (H) Ce/Ce*. The blue bars represent volcanic ash layers recognized in field, and the brown bars represent ash layers inferred on the basis of mineralogic and geochemical data. LPME = latest Permian mass extinction horizon. (For interpretation of the references to color in this figure legend, the reader is referred to the web version of this article.)

typical of ash-rich sediments above the LPME (Fig. 6A). The LPME is marked not only by a shift in the Eu/Eu* threshold characterizing ash layers but also by a major change in the relationship of most proxies to Eu/Eu*. These developments reflect fundamental changes in sediment provenance and environmental conditions in conjunction with the LPME event.

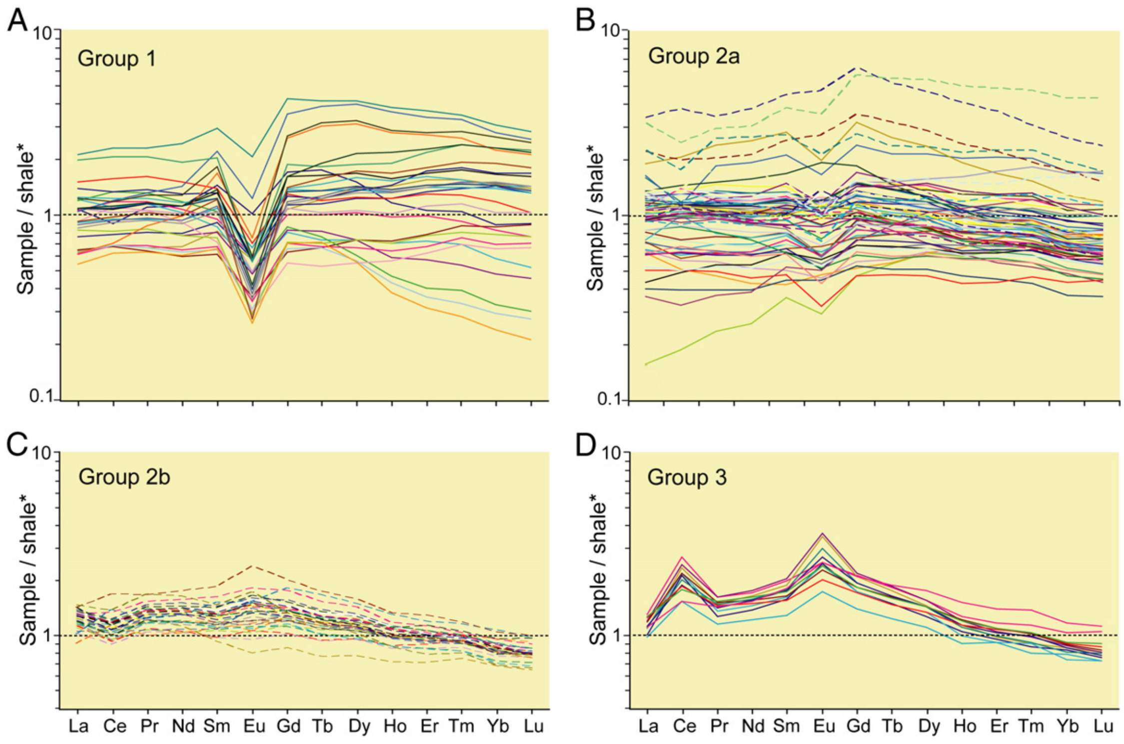

Fig. 8. REE spidergrams. Group 1 includes samples with Eu/Eu* < 0.7, Group 3 samples with Eu/Eu* and Ce/Ce* > 1.2, and Group 2 all remaining samples; Groups 2a and 2b samples are from below and above the LPME, respectively. All values represent ratios of PAAS-normalized samples (Taylor and McClennan, 1985) in log units.

Please cite this article as: Shen, J., et al., Volcanism in South China during the Late Permian and its relationship to marine ecosystem and environmental changes, Glob. Planet. Change (2012), doi:10.1016/j.gloplacha.2012.02.011

5.1.1. Marine productivity

Volcanic ashfall events may have had detrimental effects on both the phytoplankton and zooplankton communities at Xinmin. The abundance of biogenic silica (chert) covaries positively with Eu/Eu* both below and above the LPME (Fig. 9A), consistent with a decrease in siliceous plankton productivity in response to a greater flux of volcanic ash. Above the LPME, chert abundance becomes lower for a given Eu/Eu* value, a pattern we attribute to generally reduced radiolarian productivity as a consequence of environmental stresses other than direct volcanic effects, e.g., expansion of the oceanic oxygen-minimum zone (Algeo et al., 2010, 2011a; Shen et al., 2012). However, the decline in radiolarian productivity on the South China Craton appears to have been smaller than for sections from the middle of the Panthalassic Ocean: the decrease in chert abundance across the LPME is equivalent to a productivity decrease of ~20–50% at Xinmin versus ~60–90% for Japanese PTB sections (Algeo et al., 2010, 2011a). Calcite is present mainly in microcrystalline form and has an uncertain origin, but strong positive covariation with chert (Fig. 5B) suggests that it too represents a productivity signal. Below the LPME, calcite concentrations are lower in the ash layers than in the mudstone beds (Fig. 9B), and the disappearance of calcite above the LPME may represent the extinction of some unknown algal producer of calcareous sediment.

Whether primary productivity varied in response to episodic volcanic events in the South China region is more difficult to evaluate. Variations in chert abundance may be a good proxy for paleo-productivity levels owing to the dual roles of radiolarians as primary consumers dependent on phytoplankton biomass as well as hosts for symbiotic algae (Caron et al., 1995; Dennett et al., 2002). Other proxies support the hypothesis of reduced primary productivity across the South China Craton following the latest Permian crisis (Algeo et al., 2012b). First, reduced primary production during volcanic events may be indicated by variation in organic C isotopes. Pre-LPME samples show lower δ^{13}C values with increasing ash content (i.e., lower Eu/Eu*; Fig. 10A), and low δ^{13}C values can result from increased photosynthetic fractionation in a low-productivity marine system (Hinga et al., 1994). Second, TOC values at Xinmin, while ranging up to several percent below the LPME, fall to uniformly low values (<0.2%) above the LPME (Fig. 7A), which is consistent with a reduced flux of organic matter to the sediment–water interface. Sharp TOC declines across the LPME have been reported from many other PTB sections on the South China Craton (Algeo et al., 2012b).

5.1.2. Redox conditions

The relationship of redox conditions in the deep-marine environment at Xinmin to volcanic events is not entirely clear. Below the LPME, U concentrations increase in the ash layers (to a maximum of 25 ppm; Fig. 7G) and show a strong relationship to Al ($r=+0.56$), suggesting that U content is related to sediment provenance (i.e., high-U volcanic ash). However, U enrichment factors (U_{EF}) are modest (~1.5–5.0) and show little relationship to ash content (as proxied by Eu/Eu*; Fig. 10B). We interpret these patterns as evidence of generally suboxic conditions in the Xinmin environment (cf. Algeo and Tribovillard, 2009) with little redox influence by volcanic events. Above the LPME, U concentrations are uniformly close to detrital values (<5 ppm) but Mo concentrations increase episodically (to a maximum of 18 ppm) although with no apparent relationship to volcanic events (Fig. 7E). We interpret these patterns as evidence of generally more oxic conditions, with the Mo spikes developing during brief episodes of euxinia following the LPME (cf. Grice et al., 2005; Algeo et al.,

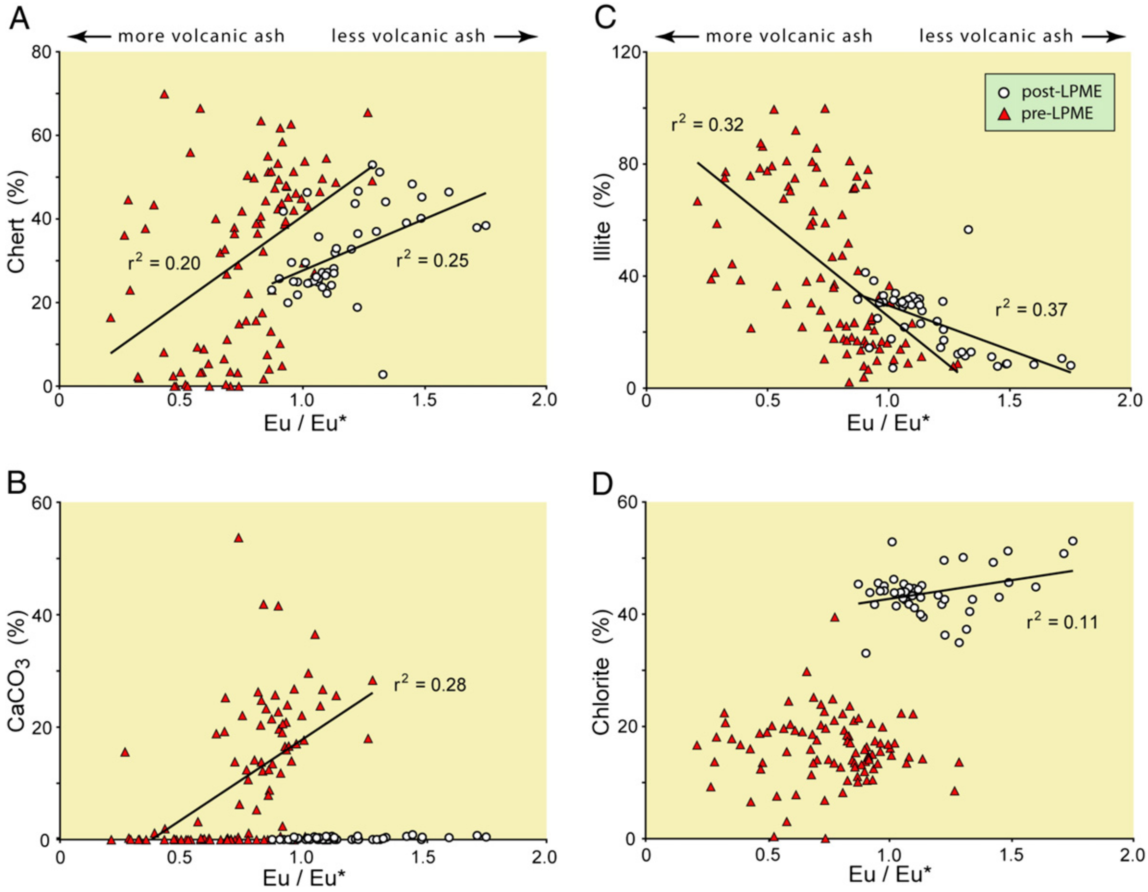

Fig. 9. Eu/Eu* versus major mineral fractions: (A) chert, (B) $CaCO_3$, (C) illite, and (D) chlorite. Arrows at top show relative influence of volcanic ash on sediment chemistry. LPME = latest Permian mass extinction.

Please cite this article as: Shen, J., et al., Volcanism in South China during the Late Permian and its relationship to marine ecosystem and environmental changes, Glob. Planet. Change (2012), doi:10.1016/j.gloplacha.2012.02.011

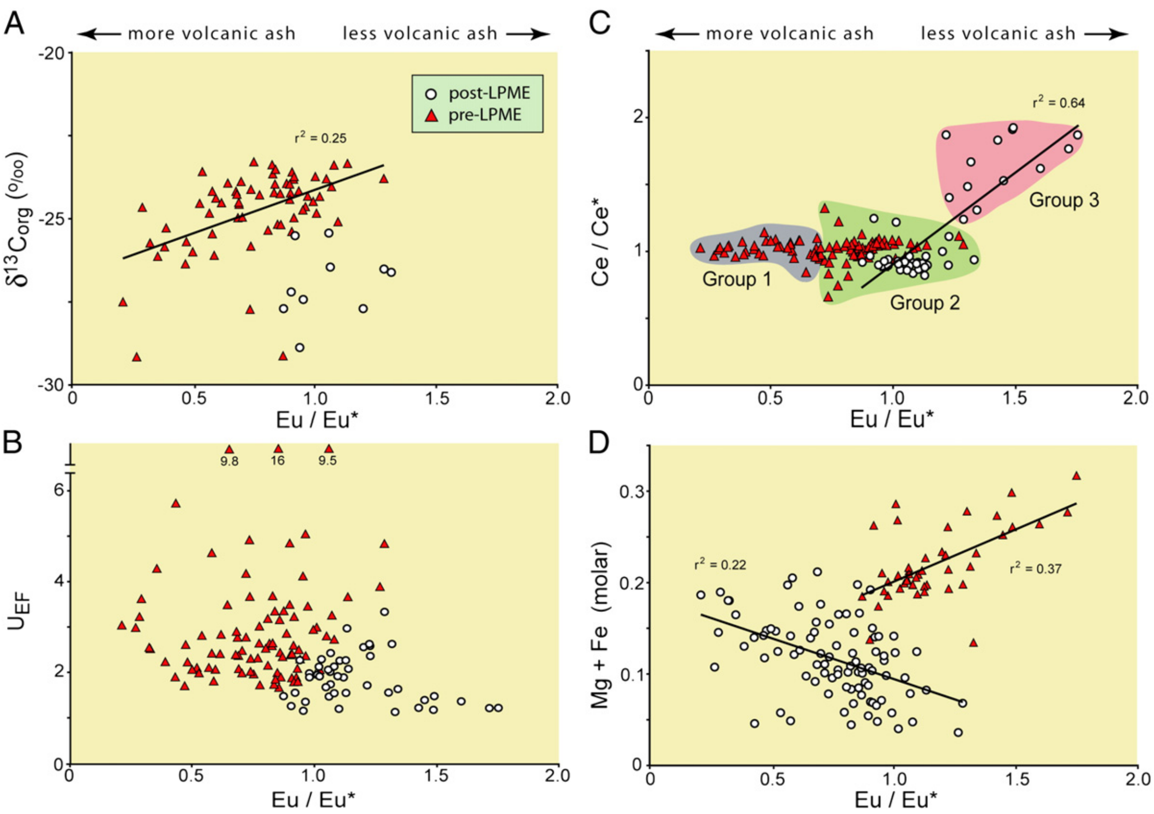

Fig. 10. Eu/Eu* versus other proxies: (A) organic δ^{13}C, (B) U_{EF}, (C) Ce/Ce*, and (D) molar Mg + Fe. Arrows at top show relative influence of volcanic ash on sediment chemistry. REE groups from Fig. 8 are shown in C. LPME = latest Permian mass extinction.

2007a, 2008). These redox interpretations are consistent with those for other deep-shelf sections from South China (e.g., Shen et al., 2012).

Information about environmental redox conditions can be provided by Ce/Ce* also. Under reducing conditions, Ce^{+3} is not fractionated from other (trivalent) lanthanide-series elements, yielding Ce/Ce* values of ~1.0. Under oxic conditions, Ce^{+4} is preferentially removed to the sediment through adsorption onto particulates (Elderfield, 1988), resulting in Ce depletion in seawater and Ce/Ce* values of $\ll$1.0. In contrast to U and Mo, which reflect local redox conditions on the seafloor (see above), Ce/Ce* provides information about redox conditions at a somewhat larger scale, e.g., within a regional watermass (Elderfield, 1988). At Xinmin, Ce/Ce* values are uniformly close to ~1.0 below the LPME (Fig. 7H), indicating either suboxic or anoxic conditions. Lack of Mo enrichment (Fig. 7E) is evidence against euxinic conditions on the Xinmin seafloor but does not preclude development of euxinia elsewhere regionally. A recent study has documented expansion of the intermediate-depth (~500–1000 m) oxygen-minimum zone within the Tethys Ocean somewhat (<100 kyr) in advance of the LPME (Shen et al., 2012). This development could account for Ce/Ce* values of ~1.0 at Xinmin despite other evidence of suboxic, rather than euxinic, local conditions.

Above the LPME, the pattern of Ce/Ce* variation changes abruptly, with implications for environmental redox conditions. The ash layers yield Ce/Ce* values of ~0.8–1.0 (Fig. 7H), consistent with suboxic conditions during volcanic ashfall events. On the other hand, the mudstone layers yield Ce/Ce* values mostly of 1.3–1.9 (Fig. 7H), consistent with oxic conditions during background sedimentation. Strong positive covariation between Ce/Ce* and ash content (as proxied by Eu/Eu*; Fig. 10C) indicates that benthic redox conditions fluctuated systematically in conjunction with ashfall events during this interval. Ce/Ce* values of $\gg$1.0 are characteristic of oxic environments in which Ce^{+4} is adsorbed onto colloidal particles that subsequently settle to the seafloor (Sholkovitz, 1992; Sholkovitz et al., 1994). This process is effective at removing Ce from the water column in modern estuaries where a high concentration of suspended particles and the mixing of watermasses of different ionic speciation promote the flocculation and settling of colloids. A similar process may have operated in cratonic marine settings following the LPME, because intensified subaerial weathering (Algeo and Twitchett, 2010) may have enhanced the riverine flux of particulate material and the potential for colloid formation in brackish interior seas.

5.1.3. Clay–mineral assemblage

The composition of the clay–mineral fraction at Xinmin varied as a function of the volcanic ash flux and changes in volcanic and detrital mineral provenance at the LPME. Illite is associated primarily with the volcanic ash layers, as shown by (1) some ash layers containing in excess of 80% illite, and (2) the mudstone layers with the smallest ash fraction (as proxied by high Eu/Eu*) containing only ~10 ± 10% illite (Fig. 9C). These observations are consistent with derivation of most illite in the study section via diagenetic transformation of volcanic ash (cf. Bethke et al., 1986; see Section 4.1). However, the chemical composition of the illitic phase appears to have changed at the LPME, as shown by an Al_2O_3/K_2O ratio of 3.49 for pre-LPME samples versus a ratio of 2.24 for post-LPME samples (Fig. 5A). This shift may have been due to a change in the composition of the volcanic ash itself, or to a change in weathering intensity following ash deposition.

Although chlorite increases substantially across the LPME (from ~15 ± 8% to ~45 ± 5%), it shows no relationship to volcanic ash content (as proxied by Eu/Eu*) for pre-LPME samples and only a marginal relationship for post-LPME samples (Fig. 9D). However, the apparent lack of a relationship among these proxies may reflect the limitations of estimating clay mineral abundances per Eqs. (1) and (2). For both pre- and post-LPME samples, chlorite shows a strong relationship to molar Mg + Fe content (Fig. 5D; Section 4.2), and molar Mg + Fe content shows a significant relationship to Eu/Eu* (Fig. 10D). Thus, it is

Please cite this article as: Shen, J., et al., Volcanism in South China during the Late Permian and its relationship to marine ecosystem and environmental changes, Glob. Planet. Change (2012), doi:10.1016/j.gloplacha.2012.02.011

logical to infer that chlorite covaried with the volcanic ash fraction, although the nature of this covariation changed across the LPME. Chlorite abundance (as proxied by molar Mg+Fe) increases with higher ash content (lower Eu/Eu*) below the LPME but decreases with higher ash content above the LPME (Fig. 10B). The volcanic endmember of both stratigraphic intervals has similar chlorite abundances (~30–40%; Fig. 5D) and molar Mg+Fe values (~0.15–0.20; Fig. 10B; cf. Masuda et al., 2001). In contrast, the non-volcanic (detrital) endmember is characterized by markedly different molar Mg+Fe values (<0.10 for pre-LPME; >0.25 for post-LPME; Fig. 10B) and chlorite abundances (<15% for pre-LPME; >45% for post-LPME; Fig. 5D), suggesting a change in the composition and, hence, the provenance of the detrital siliceous fraction at the LPME.

Further evidence for a change in the provenance of the detrital siliceous fraction at the LPME is provided by a shift in the Eu/Eu* values of the mudstone layers having minimal ash content (i.e., low illite content), from ~1.0±0.2 for pre-LPME samples to ~1.4±0.2 for post-LPME samples (Fig. 9C). This shift toward higher Eu/Eu* values may be indicative of weathering of material derived from a hydrothermal or mantle source (Taylor and McClennan, 1985). Based on the forgoing observations, we infer that the LPME was characterized by changes in (1) the provenance of the detrital siliceous fraction, and (2) either the composition of the volcanic ash fraction or its degree of weathering. Changes in sediment provenance and weathering intensity at the LPME may have been related to concurrent changes in climate and vegetation and their influence on landscape stability (see Section 5.2.3).

5.2. Relationship to global changes during the latest Permian

5.2.1. Marine productivity

The PTB crisis triggered major changes in marine phytoplankton assemblages and primary productivity levels, although the nature of these changes remains under debate. During the crisis, eukaryotic marine algae declined abruptly (Knoll et al., 2007), followed by blooms of prasinophyte and acritarch “disaster species” (Payne and van de Schootbrugge, 2007) as well as of green sulfur and N-fixing cyanobacteria (Grice et al., 2005; Xie et al., 2005, 2007; Hays et al., 2007; Cao et al., 2009; Luo et al., 2011). Changes in the composition of the phytoplanktic community may have worked to the detriment of primary consumers such as radiolarians (Feng et al., 2007; Isozaki et al., 2007; Algeo et al., 2010, 2011a; Shen et al., 2012). These patterns are supported by data from Xinmin, which document pronounced declines in biogenic silica abundance during pre-crisis volcanic events as well as at the LPME.

Changes in taxonomic diversity and community structure do not necessarily equate with changes in primary productivity rates, however. A general collapse of marine primary productivity during the Early Triassic (Martin, 1996; Rampino and Caldeira, 2005) is difficult to reconcile with evidence of (1) disproportionate survival of taxa with high rates of basal and exercise metabolism, e.g., many molluscans, (Knoll et al., 2007) and (2) widespread Early Triassic oceanic anoxia (Isozaki, 1997; Wignall and Twitchett, 2002), which may have been promoted by high levels of primary productivity following the boundary crisis (Algeo et al., 2011b). An analysis of sedimentary organic carbon fluxes across the PTB (Algeo et al., 2012b) showed little change for most regions globally, suggesting that primary productivity rates were sustained roughly at their pre-crisis levels. However, a prominent exception is the South China region, where organic carbon fluxes declined by an average factor of 3 to 6× across the LPME, probably in response to a sharp decrease in primary productivity in interior seas of the South China Craton (Algeo et al., 2012b). This decrease is recorded at Xinmin by a sharp drop in TOC concentrations at the LPME (Fig. 7A). The results of the present study may be significant in documenting a relationship between marine primary productivity and volcanic ashfall events prior to and during the PTB crisis.

5.2.2. Oceanic redox conditions

Abundant evidence documents an expansion of anoxia in the global ocean following the LPME, although the range, intensity, and persistence of such conditions remain under debate. The hypothesis of long-term deep-ocean anoxia (Isozaki, 1997; Wignall and Twitchett, 2002) is dubious given the difficulty of sustaining such conditions for longer than a few thousand years (Hotinski et al., 2001; Kiehl and Shields, 2005). Additionally, recent reanalysis of PTB deep-ocean sections has demonstrated that the Late Permian deep-ocean environment was probably suboxic rather than euxinic, and that the largest redox changes occurred not on the deep seafloor but, rather, within the oxygen-minimum zone (Algeo et al., 2010, 2011a; Wignall et al., 2010; Brennecka et al., 2011). Euxinia was widespread in shallow-marine environments but only during the latest Permian, i.e., following the LPME (Grice et al., 2005; Kakuwa and Matsumoto, 2006; Hays et al., 2007). Euxinic episodes in shallow settings appear to have been a recurrent phenomenon (Algeo et al., 2007a, 2008; Bond and Wignall, 2010) linked to expansion of the oxygen-minimum zone and transient chemocline shallowing (Kump et al., 2005).

Xinmin represents a deep-shelf setting and, thus, provides a crucial link between watermass redox conditions in the deep ocean and in shallow-marine settings. Redox conditions at Xinmin were mostly suboxic prior to the LPME, as shown by modest U enrichments (Fig. 7G) and Ce/Ce* values of ~1.0 (Fig. 7H). Following the latest Permian crisis, redox conditions were mostly oxic but punctuated by brief episodes of euxinia, as suggested by local Mo enrichments (Fig. 7E). The shift to less reducing conditions may have been brought about by a decrease in marine primary productivity and organic carbon sinking flux, as reflected in the TOC profile (Fig. 7A). Oxic conditions must have been prevalent in coastal regions of the basin following the LPME in order to effectuate removal of Ce^{+4} to the sediment, producing the observed shift to Ce/Ce* values of >1.3 (Fig. 7H). As in shallower settings, euxinia may have developed sporadically in the deep-shelf environment at Xinmin in response to chemocline shallowing.

5.2.3. Climate change and weathering fluxes

The Permian–Triassic transition was associated with major changes in terrestrial ecosystems, weathering processes, and climate. Mature gymnosperm-dominated floras were replaced by rapidly growing early successional communities dominated by lycopsids and ferns (Wang, 1996; Looy et al., 1999, 2001; Grauvogel-Stamm and Ash, 2005; Krassilov and Karasev, 2009). Widespread loss of vegetative cover contributed to massive erosion, as shown by a shift from fine-grained meandering to conglomeratic braided fluvial facies (Newell et al., 1999; Ward et al., 2000; Michaelsen, 2002), by transported soil clasts (Retallack, 2005), and by an abrupt influx of soil-derived biomarkers (Sephton et al., 2005; Xie et al., 2005, 2007; Wang and Visscher, 2007) and terrigenous siliciclastics to shallow-marine carbonate platforms (Tong et al., 2007; Algeo and Twitchett, 2010). Elevated rates of continental erosion (~7× Late Permian rates) may have continued for up to ~2 million years into the Early Triassic due to a combination of warmer conditions, acid rainfall, and disturbed landscapes (Algeo and Twitchett, 2010). These events were accompanied by major changes in climate, although the global pattern is not uniform and different regions show trends toward greater humidity or aridity in the Early Triassic (Kozur, 1998; Krassilov and Karasev, 2009; Thomas et al., 2011; Algeo et al., 2012a).

The Xinmin section records evidence of major changes in weathering processes in the South China region following the LPME. CIA values (Fig. 6C) indicate a large shift toward more humid conditions, resulting in more intense weathering of the detrital fraction. Changes in climate are known to result in changes in clay–mineral composition from a single protolith (Vogt et al., 2010). The Xinmin section also exhibits a large increase in the chlorite content of the detrital fraction (Fig. 5D) and a shift toward much higher Eu/Eu* values (Fig. 6A), indicating that the provenance of this fraction changed at the time of the LPME. Such a change may reflect the effects of

Please cite this article as: Shen, J., et al., Volcanism in South China during the Late Permian and its relationship to marine ecosystem and environmental changes, Glob. Planet. Change (2012), doi:10.1016/j.gloplacha.2012.02.011

landscape stripping in combination with increased rates of rainfall, weathering, and erosion (see above).

5.3. Sources and significance of volcanic ashfall events

The source of the volcanic ash layers found at Xinmin and other PTB sections in South China is unknown at present. Their chemistry indicates derivation from a magma of intermediate to acidic composition, probably within the South China region (Yang et al., 1991; Zhang et al., 2006). Paleogeographic details support this interpretation as well: the number and thickness of the ash layers increases toward Yunnan and Guangxi provinces (Yin et al., 1992; Feng et al., 2007; Tong et al., 2007), in a paleo-southward direction that is antipodal to the Siberian Traps volcanic centers (Fig. 1). These ash layers may have been erupted from a subduction-zone volcanic arc system along the South China–Panthalassa plate margin or another of the convergent plate margins in this region (Scotese and Langford, 1995; Stampfli and Borel, 2001). Felsic volcanism in South China continued from the Early Permian through the beginning of the Middle Triassic (Tong et al., 2005, 2007), a timeline consistent with the convergence of the eastern Tethyan microcontinents prior to the Late Triassic Indosinian Orogeny (Lepvrier et al., 2004).

The potential harmful effects of volcanic eruptions on marine biotas are illustrated by the 1991 eruption of Mount Pinatubo in the Philippines. Despite its modest size (~5.5 km^3), the Pinatubo eruption deposited an ash layer that thinned from ~10 cm proximally to a feather edge distally over an area of ~370×10^3 km^2 in the South China Sea (Wiesner et al., 1995). The ash layer induced steep declines in the abundance of benthic foraminifera and other organisms, with 100% mortality in proximal regions (Hess and Kuhnt, 1996; Hess et al., 2001; Kuhnt et al., 2005). The effects on volcanic ash on oceanic plankton communities are more poorly known. Ash can potentially have a fertilizing effect, providing nutrients such as P, Fe, and Si (Frogner et al., 2001). However, large eruptions might be expected to harm plankton through reduced light penetration, deposition of toxic trace metals, and/or acidification of surface waters by volcanic aerosols (Felitsyn and Kirianov, 2002; Sansone et al., 2002; Paytan et al., 2009). Aerosols such as SO_2 become adsorbed onto ash particles and subsequently are released upon contact with seawater, lowering seawater pH (Frogner et al., 2001). In view of the sensitivity of modern marine phytoplankton to ocean acidification (Iglesias-Rodriguez et al., 2008), this last process warrants further investigation as a possible cause of the sharp decline of Late Permian plankton communities at the LPME.

6. Conclusions

The Xinmin section provides a record of paleoceanographic conditions in a deep-shelf setting within the Nanpanjiang Basin of South China during the latest Permian. Numerous volcanic ashfall events that both preceded and followed the latest Permian marine mass extinction (LPME) resulted in significant declines in biogenic silica and carbonate production and shifts toward somewhat more reducing, but still largely suboxic, seafloor conditions. The LPME horizon also coincided with an ashfall event and shows evidence of a sharp and sustained reduction in radiolarian productivity, a shift from suboxic to mostly oxic conditions (although punctuated by episodic euxinic events), and a large increase in weathering intensity due to increased climatic humidity. Ash layers of Late Permian–Early Triassic age at Xinmin and elsewhere in South China had a regional volcanic source, perhaps in subduction-zone magmatic arcs along the margins of the South China Craton. The Xinmin section provides evidence that volcanically generated stresses that were repeatedly imposed on marine systems of the South China Craton, possibly weakening their resilience in advance of the PTB crisis.

Acknowledgments

Thanks to editor and anonymous reviewers for comments that improved the quality of this paper. We also send our thanks to Haiqiang Zhang for field work and analysis in the Laboratory. This work was supported by NSFC (project nos. 40839903, 40921062, 40972002 and 41073007), the 973 program (grant 2011CB808800), Ministry of Education of China (IRT0441 and B07039), the 111 program (B08030), and the U.S. National Science Foundation (grants EAR-0618003, EAR-0745574, and EAR-1053449 to TJA). This paper is a contribution to IGCP Project 572.

References

Algeo, T.J., Tribovillard, N., 2009. Environmental analysis of paleoceanographic systems based on molybdenum–uranium covariation. Chemical Geology 268, 211–225.

Algeo, T.J., Twitchett, R.J., 2010. Anomalous Early Triassic sediment fluxes due to elevated weathering rates and their biological consequences. Geology 38, 1023–1026.

Algeo, T.J., Ellwood, B.B., Nguyen, T.K.T., Rowe, H., Maynard, J.B., 2007a. The Permian–Triassic boundary at Nhi Tao, Vietnam: evidence for recurrent influx of sulfidic watermasses to a shallow-marine carbonate platform. Palaeogeography, Palaeoclimatology, Palaeoecology 252, 304–327.

Algeo, T.J., Hannigan, R., Rowe, H., Brookfield, M., Baud, A., Krystyn, L., Ellwood, B.B., 2007b. Sequencing events across the Permian–Triassic boundary, Guryul Ravine (Kashmir, India). Palaeogeography, Palaeoclimatology, Palaeoecology 252, 328–346.

Algeo, T.J., Shen, Y.N., Zhang, T.G., Lyons, T., Bates, S., Rowe, H., Nguyen, T.K.T., 2008. Association of ^{34}S-depleted pyrite layers with negative carbonate δ^{13}C excursions at the Permian/Triassic boundary: evidence for upwelling of sulfidic deep-ocean watermasses. Geochemistry Geophysics Geosystems 9 Q04025, 10 pp..

Algeo, T.J., Hinnov, L., Moser, J., Maynard, J.B., Elswick, E., Kuwahara, K., Sano, H., 2010. Changes in productivity and redox conditions in the Panthalassic Ocean during the latest Permian. Geology 38, 187–190.

Algeo, T.J., Chen, Z.Q., Fraiser, M.L., Twitchett, R.J., 2011a. Terrestrial–marine teleconnections in the collapse and rebuilding of Early Triassic marine ecosystems. Palaeogeography, Palaeoclimatology, Palaeoecology 308, 1–11.

Algeo, T.J., Kuwahara, K., Sano, H., Bates, S., Lyons, T., Elswick, E., Hinnov, L., Ellwood, B.B., Moser, J., Maynard, J.B., 2011b. Spatial variation in sediment fluxes, redox conditions, and productivity in the Permian–Triassic Panthalassic Ocean. Palaeogeography, Palaeoclimatology, Palaeoecology 308, 65–83.

Algeo, T.J., Henderson, C.M., Ellwood, B.B., Rowe, H., Elswick, E., Bates, S., Lyons, T., Hower, J.C., Smith, C., Maynard, B., Hays, L., Summons, R., Fulton, J., Freeman, K., 2012. Evidence for a diachronous Late Permian marine crisis from the Canadian Arctic region. Geological Society of America Bulletin, http://dx.doi.org/10.1130/B30505.1 publ. online 6 February.

Algeo, T.J., Henderson, C.M., Tong, J.N., Feng, Q.L., Yin, H.F., Tyson, R.V., this volume. Plankton and productivity during the Permian–Triassic boundary crisis: an analysis of organic carbon fluxes. Global and Planetary Change.

Baud, A., Holser, W.T., Magaritz, M., 1989. Permian–Triassic of the Tethys; carbon isotope studies. Geologische Rundschau 78, 649–677.

Bethke, C.M., Vergo, N., Altaner, S.P., 1986. Pathways of smectite illitization. Clays and Clay Minerals 34, 125–135.

Bond, D.P.G., Wignall, P.B., 2010. Pyrite framboid study of marine Permian–Triassic boundary sections: a complex anoxic event and its relationship to contemporaneous mass extinction. Geological Society of America Bulletin 122, 1265–1279.

Brennecka, G.A., Herrmann, A.D., Algeo, T.J., Anbar, A.D., 2011. Rapid expansion of oceanic anoxia immediately before the end-Permian mass extinction. Proceedings of the National Academy of Sciences (USA) 108, 17631–17634.

Campbell, I.H., Czamanske, G.K., Fedorenko, V.A., Hill, R.I., Stepanov, V., 1992. Synchronism of the Siberian Traps and the Permian–Triassic boundary. Science 258, 1760–1763.

Cao, C.Q., Love, G.D., Hays, L.E., Wang, W., Shen, S., Summons, R.E., 2009. Biogeochemical evidence for euxinic oceans and ecological disturbance presaging the end-Permian mass extinction event. Earth and Planetary Science Letters 281, 188–201.

Caron, D.A., Michaels, A.F., Swanberg, N.R., Howse, F.A., 1995. Primary productivity by symbiont-bearing planktonic sarcodines (Acantharia, Radiolaria, Foraminifera) in surface waters near Bermuda. Journal of Plankton Research 17, 103–129.

DeMaster, D.J., 2004. The diagenesis of biogenic silica; chemical transformations occurring in the water column, seabed, and crust. In: Turekian, K.K. (Ed.), Sediments, Diagenesis, and Sedimentary Rocks. Elsevier-Pergamon, Oxford, pp. 87–98.

Dennett, M.R., Caron, D.A., Michaels, A.F., Gallager, S.M., Davis, C.S., 2002. Video plankton recorder reveals high abundances of colonial Radiolaria in surface waters of the central North Pacific. Journal of Plankton Research 24, 797–805.

Drits, V.A., Sakharov, B.A., Lindgreen, H., Salyn, A.L., 1997. Sequential structural transformation of illite–smectite–vermiculite during diagenesis of Upper Jurassic shales from the North Sea and Denmark. Clay Minerals 32, 351–371.

Elderfield, H., 1988. The oceanic chemistry of the rare-earth elements. Philosophical Transactions of the Royal Society of London A 325, 105–126.

Ellwood, B.B., Crick, R.E., El Hassani, A., Benoist, S., Young, R.H., 2000. Magnetosusceptibility event and cyclostratigraphy method applied to marine rocks: detrital input versus carbonate productivity. Geology 28, 1135–1138.

Ellwood, B.B., Tomkin, J.K., Ratcliffe, K.T., Wright, M., Kafafy, A.M., 2008. High-resolution magnetic susceptibility and geochemistry for the Cenomanian/Turonian boundary GSSP with correlation to time equivalent core. Palaeogeography, Palaeoclimatology, Palaeoecology 26, 105–126.

Please cite this article as: Shen, J., et al., Volcanism in South China during the Late Permian and its relationship to marine ecosystem and environmental changes, Glob. Planet. Change (2012), doi:10.1016/j.gloplacha.2012.02.011

Enos, P., Lehrmann, D.J., Wei, J., Yu, Y., Xiao, J., Chaikin, D.H., Minzoni, M., Berry, A.K., Montgomery, P., 2006. Triassic evolution of the Yangtze Platform in Guizhou Province, People's Republic of China. Geological Society of America Special Paper, 417. 105 pp.

Erwin, D.H., Bowring, S.A., Jin, Y.-G., 2002. End-Permian mass-extinctions: a review. In: Koeberl, C., MacLeod, K.G. (Eds.), Catastrophic Events and Mass Extinctions: Impacts and Beyond: Geological Society of America Special Paper, 356, pp. 353–383.

Felitsyn, S.B., Kirianov, V.Y., 2002. Mobility of phosphorus during the weathering of volcanic ashes. Lithology and Mineral Resources 37, 275–278.

Feng, Q., Gu, S., 2002. Uppermost Changxingian (Permian) radiolarian fauna from southern Guizhou, southwestern China. Journal of Paleontology 76, 797–809.

Feng, Q.L., He, W.H., Gu, S.Z., Meng, Y.Y., Jin, Y.X., Zhang, F., 2007. Radiolarian evolution during the latest Permian in South China. Global and Planetary Change 55, 177–192.

Frogner, P., Gíslason, S.R., Óskarsson, N., 2001. Fertilizing potential of volcanic ash in ocean surface water. Geology 29, 487–490.

Grauvogel-Stamm, L., Ash, S.R., 2005. Recovery of the Triassic land flora from the end-Permian life crisis. Comptes Rendus Palevol 4, 593–608.

Grice, K., Cao, C.Q., Love, G.D., Böttcher, M.E., Twitchett, R.J., Grosjean, E., Summons, R.E., Turgeon, S.C., Dunning, W., Jin, Y.G., 2005. Photic zone euxinia during the Permian–Triassic superanoxic event. Science 307, 706–709.

Grim, R.E., 1968. Clay Mineralogy, 2nd ed. McGraw-Hill, New York. 596 pp.

Hays, L.E., Beatty, T., Henderson, C.M., Love, G.D., Summons, R.E., 2007. Evidence for photic zone euxinia through the end-Permian mass extinction in the Panthalassic Ocean (Peace River Basin, Western Canada). Palaeoworld 16, 39–50.

He, W.H., Shen, S.Z., Feng, Q.L., Gu, S.Z., 2005. A late Changhsingian (Late Permian) deepwater brachiopod fauna from the Talung Formation at the Dongpan section, southern Guangxi, South China. Journal of Paleontology 79, 927–938.

Hess, S., Kuhnt, W., 1996. Deep-sea benthic foraminiferal recolonization of the 1991 Mt. Pinatubo ash layer in the South China Sea. Marine Micropaleontology 28, 171–197.

Hess, S., Kuhnt, W., Hill, S., Kaminski, M.A., Holbourn, A., de Leon, M., 2001. Monitoring the recolonization of the Mt. Pinatubo 1991 ash layer by benthic foraminifera. Marine Micropaleontology 43, 119–142.

Hinga, K.R., Arthur, M.A., Pilson, M.E.Q., Whitaker, D., 1994. Carbon isotope fractionation by marine phytoplankton in culture: the effects of CO_2 concentration, pH, temperature, and species. Global Biogeochemical Cycles 8, 91–102.

Hodder, A.P.W., Naish, T.R., Nelson, C.S., 1993. A two-stage model for the formation of smectite from detrital volcanic glass under shallow-marine conditions. Marine Geology 109, 279–285.

Horacek, M., Richoz, S., Brandner, R., Krystyn, L., Spötl, C., 2007. Evidence for recurrent changes in Lower Triassic oceanic circulation of the Tethys: the $\delta^{13}C$ record from marine sections in Iran. Palaeogeography, Palaeoclimatology, Palaeoecology 252, 355–369.

Hotinski, R.M., Bice, K.L., Kump, L.R., Najjar, R.G., Arthur, M.A., 2001. Ocean stagnation and end-Permian anoxia. Geology 29, 7–10.

Huff, W.D., Anderson, T.B., Rundle, C.C., Odin, G.S., 1991. Chemostratigraphy, K–Ar ages and illitization of Silurian K-bentonites from the Central Belt of the Southern Uplands–Down-Longford terrane, British Isles. Journal of the Geological Society of London 148, 861–868.

Huff, W.D., Bergström, S.M., Kolata, D.R., 2000. Silurian K-bentonites of the Dnestr Basin, Podolia, Ukraine. Journal of the Geological Society of London 157, 493–504.

Iglesias-Rodriguez, M.D., Halloran, P.R., Rickaby, R.E.M., Hall, I.R., Colmenero-Hidalgo, E., Gittins, J.R., Green, D.R.H., Tyrrell, T., Gibbs, S.J., von Dassow, P., Rehm, E., Armbrust, E.V., Boessenkool, K.P., 2008. Phytoplankton calcification in a high-CO_2 world. Science 320, 336–340.

Isozaki, Y., 1997. Triassic boundary superanoxia and stratified superocean: records from lost deep sea. Science 276, 235–238.

Isozaki, Y., Shimizu, N., Yao, J., Ji, Z., Matsuda, T., 2007. End-Permian extinction and volcanism-induced environmental stress: Permian–Triassic boundary interval of a lower-slope facies at Chaotian, South China. Palaeogeography, Palaeoclimatology, Palaeoecology 252, 218–238.

Jin, Y.G., Wang, Y., Wang, W., Shang, Q.H., Cao, C.Q., Erwin, D.H., 2000. Pattern of marine mass extinction near the Permian–Triassic boundary in South China. Science 289, 432–436.

Kakuwa, Y., Matsumoto, R., 2006. Cerium negative anomaly just before the Permian and Triassic boundary event: the upward expansion of anoxia in the water column. Palaeogeography, Palaeoclimatology, Palaeoecology 229, 335–344.

Kamo, S.L., Czamanske, G.K., Amelin, Y., Fedorenko, V.A., Davis, D.W., Trofimov, V.R., 2003. Rapid eruption of Siberian flood-volcanic rocks and evidence for coincidence with the Permian–Triassic boundary and mass extinction at 251 Ma. Earth and Planetary Science Letters 214, 75–91.

Kiehl, J.T., Shields, C.A., 2005. Climate simulation of the latest Permian: implications for mass extinction. Geology 33, 757–760.

Knoll, A.H., Bambach, R.K., Payne, J.L., Pruss, S.B., Fischer, F., 2007. Paleophysiology and end-Permian mass extinction. Earth and Planetary Science Letters 256, 295–313.

Kozur, H.W., 1998. Some aspects of the Permian–Triassic boundary (PTB) and of the possible causes for the biotic crisis around this boundary. Palaeogeography, Palaeoclimatology, Palaeoecology 143, 227–272.

Krassilov, V., Karasev, E., 2009. Paleofloristic evidence of climate change near and beyond the Permian–Triassic boundary. Palaeogeography, Palaeoclimatology, Palaeoecology 284, 326–336.

Kuhnt, W., Hess, S., Holbourn, A., Paulsen, H., Salomon, B., 2005. The impact of the 1991 Mt. Pinatubo eruption on deep-sea foraminiferal communities: a model for the Cretaceous–Tertiary (K/T) boundary? Palaeogeography, Palaeoclimatology, Palaeoecology 224, 83–107.

Kump, L.R., Pavlov, A., Arthur, M.A., 2005. Massive release of hydrogen sulfide to the surface ocean and atmosphere during intervals of oceanic anoxia. Geology 33, 397–400.

Lai, X.L., Wignall, P.B., Zhang, K.X., 2001. Palaeoecology of the conodonts *Hindeodus* and *Clarkina* during the Permian–Triassic transitional period. Palaeogeography, Palaeoclimatology, Palaeoecology 171, 63–72.

Lepvrier, C., Leyreloup, A., Maluski, H., Vuong, N.V., Thi, P.T., Tich, V.T., 2004. The Early Triassic Indosinian Orogeny in Vietnam (Truong Son Belt and Kontum Massif); implications for the geodynamic evolution of Indochina. Tectonophysics 393, 87–118.

Looy, C.V., Brugman, W.A., Dilcher, D.L., Visscher, H., 1999. The delayed resurgence of equatorial forests after the Permian–Triassic ecological crisis. Proceedings of the National Academy of Sciences U. S. A. 96, 13857–13862.

Looy, C.V., Twitchett, R.J., Dilcher, D.L., van Konijnenburg-van Cittert, J.H.A., Visscher, H., 2001. Life in the end-Permian dead zone. Proceedings of the National Academy of Sciences U. S. A. 98, 7879–7883.

Luo, G.M., Wang, Y.B., Kump, L.R., Bai, X., Algeo, T.J., Yang, H., Xie, S.C., 2011. Nitrogen fixation prevailed simultaneously with the end-Permian marine mass extinction and its implications. Geology 39, 647–650.

Lyons, T.W., Severmann, S., 2006. A critical look at iron paleoredox proxies: new insights from modern euxinic marine basins. Geochimica et Cosmochimica Acta 70, 5698–5722.

Martin, R.E., 1996. Secular increase in nutrient levels through the Phanerozoic: implications for productivity, biomass, and diversity of the marine biosphere. Palaios 11, 209–219.

Masuda, H., Peacor, D.R., Dong, H., 2001. Transmission electron microscopy study of conversion of smectite to illite in mudstones of the Nankai Trough; contrast with coeval bentonites. Clays and Clay Minerals 49, 109–118.

Michaelsen, P., 2002. Mass extinction of peat-forming plants and the effect on fluvial styles across the Permian–Triassic boundary, northern Bowen Basin, Australia. Palaeogeography, Palaeoclimatology, Palaeoecology 179, 173–188.

Newell, A.J., Tverdokhlebov, V.P., Benton, M.J., 1999. Interplay of tectonics and climate on a transverse fluvial system, Upper Permian, Southern Uralian Foreland Basin, Russia. Sedimentary Geology 127, 11–29.

Payne, J., van de Schootbrugge, B., 2007. Life in Triassic oceans: links between benthic and planktonic recovery and radiation. In: Falkowski, P.G., Knoll, A.H. (Eds.), The Evolution of Primary Producers in the Sea. Academic Press, New York, pp. 165–189.

Paytan, A., Mackey, K.R.M., Chen, Y., Lima, I.D., Doney, S.C., Mahowald, N., Labiosa, R., Post, A.F., 2009. Toxicity of atmospheric aerosols on marine phytoplankton. Proceedings of the National Academy of Sciences U. S. A. 106, 4601–4605.

Price, J.R., Velbel, M.A., 2003. Chemical weathering indices applied to weathering profiles developed on heterogeneous felsic metamorphic parent rocks. Chemical Geology 202, 397–416.

Rampino, M.R., Caldeira, K., 2005. Major perturbation of ocean chemistry and a “Strangelove Ocean” after the end-Permian mass extinction. Terra Nova 17, 554–559.

Reichow, M.K., Pringle, M.S., Al'Mukhamedov, A.I., Allen, M.B., Andreichew, V.L., Buslov, M.M., Davies, C.E., Fedoseev, G.S., Fitton, J.G., Inger, S., Medvedev, A.Y., Mitchell, C., Puchkov, V.N., Safanova, I.Y., Scott, R.A., Saunders, A.D., 2009. The timing and extent of the eruption of the Siberian Traps large igneous province: implications for the end-Permian environmental crisis. Earth and Planetary Science Letters 277, 9–20.

Renne, P.R., Zheng, Z.C., Richards, M.A., Black, M.T., Basu, A.R., 1995. Synchrony and causal relations between Permian–Triassic boundary crisis and Siberian flood volcanism. Science 269, 1413–1416.

Retallack, G.J., 2005. Earliest Triassic claystone breccias and soil-erosion crisis. Journal of Sedimentary Research 75, 679–695.

Sansone, F.J., Benitez-Nelson, C.R., Resing, J.A., DeCarlo, E.H., Vink, S.M., Heath, J.A., Huebert, B.J., 2002. Geochemistry of atmospheric aerosols generated from lava–seawater interactions. Geophysical Research Letters 29, 1335 4 pp.

Scotese, C.R., Langford, R.P., 1995. Pangea and the paleogeography of the Permian. In: Scholle, P.A., Peryt, T.M., Ulmer-Scholle, D.S. (Eds.), The Permian of Northern Pangea, v. 1: Paleogeography, Paleoclimates, Stratigraphy. Springer-Verlag, Berlin, pp. 3–19.

Sephton, M.A., Looy, C.V., Brinkhuis, H., Wignall, P.B., de Leeuw, J.W., Visscher, H., 2005. Catastrophic soil erosion during the end-Permian biotic crisis. Geology 33, 941–944.

Shen, J., Algeo, T.J., Zhou, L., Feng, Q.L., Yu, J.X., Ellwood, B.B., 2012. Volcanic perturbations of the marine environment in South China preceding the latest Permian extinction event and their biotic effects. Geobiology 10, 82–103.

Sholkovitz, E.R., 1992. Chemical evolution of rare earth elements: fractionation between colloidal and solution phases of filtered river water. Earth and Planetary Science Letters 114, 77–84.

Sholkovitz, E.R., Landing, W.M., Lewis, B.L., 1994. Ocean particle chemistry: the fractionation of rare earth elements between suspended particles and seawater. Geochimica et Cosmochimica Acta 58, 1567–1579.

Srodon, J., 2009. Quantification of illite and smectite and their layer charges in sandstones and shales from shallow burial depth. Clay Minerals 44, 421–434.

Srodon, J., Drits, V.A., McCarty, D.K., Hsieh, J.C.C., Eberl, D.D., 2001. Quantitative XRD analysis of clay-rich rocks from random preparations. Clays and Clay Minerals 49, 514–528.

Stampfli, G.M., Borel, G.D., 2001. A plate tectonic model for the Paleozoic and Mesozoic constrained by dynamic plate boundaries and restored synthetic oceanic isochrones. Earth and Planetary Science Letters 196, 17–33.

Swartzendruber, L.J., 1992. Properties, units and constants in magnetism. Journal of Magnetic Materials 100, 573–575.

Taylor, S.R., McClennan, S.M., 1985. The Continental Crust: Its Composition and Evolution. Blackwell Scientific Publications, Oxford. 312 pp.

Please cite this article as: Shen, J., et al., Volcanism in South China during the Late Permian and its relationship to marine ecosystem and environmental changes, Glob. Planet. Change (2012), doi:10.1016/j.gloplacha.2012.02.011

Thomas, S.G., Tabor, N.J., Yang, W., Myers, T.S., Yang, Y., Wang, D., 2011. Palaeosol stratigraphy across the Permian–Triassic boundary, Bogda Mountains, NW China: implications for palaeoenvironmental transition through Earth's largest mass extinction. Palaeogeography, Palaeoclimatology, Palaeoecology 308, 41–64.

Tong, J., Hans, J., Zhao, L.S., Zuo, J.X., 2005. High-resolution Induan–Olenekian boundary sequence in Chaohu, Anhui Province. Science in China Series D 48, 291–297.

Tong, J., Zhang, S.X., Zuo, J.X., Xiong, X.Q., 2007. Events during Early Triassic recovery from the end-Permian extinction. Global and Planetary Change 55, 66–80.

Vogt, T., Clauer, N., Larque, P., 2010. Impact of climate and related weathering processes on the authigenesis of clay minerals; examples from the circum-Baikal region, Siberia. Catena 80, 53–64.

Wang, Z.Q., 1996. Recovery of vegetation from the terminal Permian mass extinction in North China. Review of Palaeobotany and Palynology 91, 121–142.

Wang, C.J., Visscher, H., 2007. Abundance anomalies of aromatic biomarkers in the Permian–Triassic boundary section at Meishan, China — evidence of end-Permian terrestrial ecosystem collapse. Palaeogeography, Palaeoclimatology, Palaeoecology 252, 291–303.

Ward, P.D., Montgomery, D.R., Smith, R., 2000. Altered river morphology in South Africa related to the Permian–Triassic extinction. Science 289, 1740–1743.

Wiesner, M.G., Wang, Y., Zheng, L., 1995. Fallout of volcanic ash to the deep South China Sea induced by the 1991 eruption of Mount Pinatubo (Philippines). Geology 23, 885–888.

Wignall, P.B., Twitchett, R.J., 2002. Extent, duration, and nature of the Permian–Triassic superanoxic event. In: Koeberl, C., MacLeod, K.G. (Eds.), Catastrophic Events and Mass Extinctions: Impacts and Beyond: Geological Society of America Special Paper, 356, pp. 395–413.

Wignall, P.B., Bond, D.P.G., Kuwahara, K., Kakuwa, Y., Newton, R.J., Poulton, S.W., 2010. An 80 million year oceanic redox history from Permian to Jurassic pelagic sediments of the Mino–Tamba terrane, SW Japan, and the origin of four mass extinctions. Global and Planetary Change 71, 109–123.

Xie, S.C., Pancost, R.D., Yin, H.F., Wang, H.M., Evershed, R.P., 2005. Two episodes of microbial change coupled with Permo/Triassic faunal mass extinction. Nature 434, 494–497.

Xie, S.C., Pancost, R.D., Huang, J.H., Wignall, P.B., Yu, J.X., Tang, X.Y., Chen, L., Huang, X.Y., Lai, X.L., 2007. Changes in the global carbon cycle occurred as two episodes during the Permian–Triassic crisis. Geology 35, 1083–1086.

Xie, S.C., Pancost, R.D., Wang, Y.B., Yang, H., Wignall, P.B., Luo, G.M., Jia, C.L., Chen, L., 2010. Cyanobacterial blooms tied to volcanism during the 5 M.y. Permo-Triassic biotic crisis. Geology 38, 447–450.

Yang, Z.Y., Yin, H.F., Wu, S.B., 1987. Permian–Triassic Boundary Stratigraphy and Fauna of South China. Geological Publishing House, Beijing. 32 pp. (in Chinese).

Yang, Z.Y., Wu, S.B., Yin, H.F., Xu, G.R., Zhang, K.X., Bi, X.M., 1991. Permo-Triassic Events of South China. Geological Publishing House, Beijing. 64 pp. (in Chinese).

Yin, H.F., Huang, S.J., Zhang, K.X., Hansen, H.J., Yang, F.Q., Ding, M.H., Bie, X.M., 1992. The effects of volcanism on the Permo-Triassic mass extinction in South China. In: Sweet, W.C., Yang, Z., Dickins, J.M., Yin, H. (Eds.), Permo-Triassic Events in the Eastern Tethys. Cambridge University Press, Cambridge, pp. 146–157.

Yin, H.F., Zhang, K.X., Tong, J.N., Yang, Z.Y., Wu, S.B., 2001. The global stratotype section and point (GSSP) of the Permian–Triassic boundary. Episodes 24, 102–114.

Yin, H.F., Feng, Q.L., Lai, X.L., Baud, A., Tong, J.N., 2007. The protracted Permo-Triassic crisis and multi-episode extinction around the Permian–Triassic boundary. Global and Planetary Change 55, 1–20.

Zhang, S.X., Feng, Q.L., Gu, S.Z., Yu, J.S., 2006. Claystone around deep water Permian–Triassic boundary from the Guizhou and Guangxi region. Geological Science and Technology Information 25, 9–13 (in Chinese).

Please cite this article as: Shen, J., et al., Volcanism in South China during the Late Permian and its relationship to marine ecosystem and environmental changes, Glob. Planet. Change (2012), doi:10.1016/j.gloplacha.2012.02.011